Journal Pre-proof

Kinematics of fault-propagation folding: Analysis of velocity fields in numerical modeling simulations

Berenice Plotek, Esther Heckenbach, Sascha Brune, Ernesto Cristallini, Jeremías Likerman

PII: S0191-8141(22)00195-X

DOI: https://doi.org/10.1016/j.jsg.2022.104703

Reference: SG 104703

To appear in: *Journal of Structural Geology*

Received Date: 3 January 2022

Revised Date: 2 August 2022

Accepted Date: 12 August 2022

Please cite this article as: Plotek, B., Heckenbach, E., Brune, S., Cristallini, E., Likerman, Jeremí., Kinematics of fault-propagation folding: Analysis of velocity fields in numerical modeling simulations, *Journal of Structural Geology* (2022), doi: https://doi.org/10.1016/j.jsg.2022.104703.

Kinematics of fault-propagation folding: analysis of velocity fields in numerical modeling simulations

Berenice Plotek[a]*; Esther Heckenbach[b,c], Sascha Brune[b,c], Ernesto Cristallini[a,], Jeremías Likerman[a]

a Laboratorio de Modelado Geológico (LaMoGe), Instituto de Estudios Andinos "Don Pablo Groeber" (IDEAN), Universidad de Buenos Aires-CONICET. E-mail address: berenice@gl.fcen.uba.ar, ernesto@gl.fcen.uba.ar, jlikerman@gl.fcen.uba.ar. Postal Address: Intendente Guiraldes 2160, Ciudad Autónoma de Buenos Aires -C1428EHA, Argentina. Telephone number: + 54 (011) 5285-8248

b GFZ German Research Centre for Geosciences, Potsdam, Germany. E-mail addresses: hecken@gfz-potsdam.de, sascha.brune@gfz-potsdam.de. Postal address: Telegrafenberg, Potsdam, 14473, Germany

c Institute of Geosciences, University of Potsdam, Potsdam, Germany

Abstract:

Fault-propagation folding occurs when a shallow fold is created by an underlying propagating thrust fault. These structures are common features of fold and thrust belts and hold key economic relevance as groundwater or hydrocarbon reservoirs. Reconstructing a fault-propagation fold is commonly done by means of the trishear model of the forelimb, a theoretical approach that assumes simplistic rheological rock properties. Here we present a series of numerical models that elucidate the kinematics of fault-propagation folding within an anisotropic sedimentary cover using complex visco-elasto-plastic rheologies. We explore the influence of different parameters like cohesion, angle of internal friction, and viscosity during folding and compare the velocity field with results from the purely kinematic trishear model. In the trishear paradigm, fault-propagation folding features a triangular shear zone ahead of the fault tip whose width is defined by the apical angle that in practice serves as a freely tunable fitting parameter. In agreement with this framework, a triangular zone of concentrated strain forms in all numerical models. We use our models to relate the apical angle to the rheological properties of the modeled sedimentary layers. In purely visco-plastic models, the geometry of the forelimb obtained can be approximated using a trishear kinematic model with high apical angles ranging between 60° and 70°. However, additionally accounting for elastic deformation produces a significant change in the geometry of the beds that require lower apical angles (25°) for trishear kinematics. We conclude that all analyzed numerical models can be represented by applying the theoretical trishear model, whereby folds involving salt layers require high apical angle values while more competent sedimentary rocks need lower values.

Keywords:

Fault-propagation folds

Trishear kinematics

Numerical modeling

Velocity fields

Fault-related folding

1. Introduction:

Some thrust faults propagate gradually to the surface and, as slip accumulates, these faults develop a fault-propagation fold above their tip (Figure 1). This type of structure forms as a consequence of variations in the slip along the fault where a decrease in slip is compensated by folding of material above the fault (Suppe and Medwedeff 1990, Brandes and Tanner 2014). First kinematic models to address the evolution of fault-propagation folds (Chester and Chester 1990, Mitra 1990, Suppe and Medwedeff 1990) were based on the parallel kink-fold mechanism and allowed examination of the trajectory of the materials during folding (Dewey 1965, Maillot and Leroy 2006). However, fault-propagation folds observed in nature (Figure 1A) usually display variations in stratigraphic thickness, footwall synclines, and changes in the forelimb inclinations that are inconsistent with simple parallel kink-fold kinematics (Figure 1) (Suppe and Medwedeff 1990, Allmendinger 1998).

Trishear, an alternative kinematic model, can explain these observations (Erslev 1991, Allmendinger 1998, Coleman et al. 2019) that cannot be explained by kink-fold kinematics. This theoretical model is characterized by a distribution of the deformation within a triangular zone located immediately above the tip-line of the fault (Hardy and Ford 1997, Cristallini and Allmendinger 2001, Jabbour et al. 2012). Note that the trishear model is based on the assumption that deformation occurs only in the triangular shear zone, while in the hanging wall the particles experience rigid translation.

Fault-propagation folds have been studied with numerical modeling using finite-element methods (Braun and Sambridge 1994, Khalifeh - Soltani et al. 2021), discrete-element techniques (Finch et al. 2002, Finch et al. 2004, Hughes and Shaw 2015) and boundary element modeling (Johnson 2018). These mechanically-based models require an initial geometry in 2D or 3D of stratigraphic units and/or faults (Guzofski et al. 2009, Granado and Ruh 2019) as input, as well as rheological information about the materials involved (Ruh 2020, Huang et al. 2020, Granado et al. 2021). Cardozo et al. (2003) showed that if incompressible materials are used, the resulting fold geometries, velocity fields, and finite strain are very similar to those produced by the trishear kinematic model. Previous studies have shown that fault-propagation into the cover is strongly favored by homogeneous cover sequences (Hardy and Finch 2007) and that the strength of bedding contacts, the thickness and stiffness of layering as well as the fault geometry, all contribute significantly to the resulting shape of the fold (Johnson 2018).

Insert Figure 1 here

Numerical models can help deciphering the kinematics involved in fold formation and migration, providing a dynamic understanding of these structures. Here, we aim to understand fault-propagation folds by means of finite-element modeling. This numerical approach is available in a variety of current research software packages and has been widely applied to model complex crustal deformation, both in compression (e.g., Ruh et al. 2012, Erdős et al. 2019, Ballato et al. 2019) and extension (e.g., Van Wijk and Cloetingh 2002, Jourdon et al. 2021, Richter et al. 2021). In particular, mechanical-based numerical modeling is a very powerful tool for investigating processes associated with the formation and evolution of geological features on small and large scales (Sanz et al. 2007, Albertz and Lingrey 2012, Brune and Autin 2013, Gray et al. 2014, Brune et al. 2016).

In this study we analyze numerical examples of simple fault-propagation folds, where folding affects three different lithologies. We show that the general configuration of the resulting folding can be approximated by the trishear kinematic method, even when plasticity parameters and viscosity of the beds vary significantly. We analyze the evolution of the kinematic field and strain rate during the process of folding and faulting and compare a series of modeled kinematic fields and their geometries to theoretical trishear shape and velocity fields obtained from the Andino 3D software (Cristallini et al. 2021, Plotek et al. 2021). We find that setups where weak, salt-like layers are included, and realistic dislocation creep parameters are used develop more heterogeneous velocity distributions. In the following section, we will first review the trishear kinematic model. Next, we will present the numerical models performed, and finally, we discuss our results and their implications.

2. The trishear kinematic model

The first kinematic models to balance fault-propagation folds were based on geometrical relationships (Suppe and Medwedeff 1990, Saffar 1993). They imply ideal geometries where the main fault has a planar surface, and a kink band migration occurs during fold evolution (Woodward 1997, Jabbour et al. 2012). The trishear kinematic model was first proposed by Erslev (1991). In this theoretical model, fault-propagation folds have a triangular zone of heterogeneous deformation, surrounding the fault tip that can be modeled by non-parallel shear (Figures 1C & 1D). Originally, the only distortion and rotation in the system takes place in a triangular zone ahead of the fault tip. Brandenburg (2013) presented a modification of the trishear model where faults are treated as continuously curved.

The trishear process can generate several characteristics of fault-propagation folds, such as the curved shapes of folds and the presence of footwall synclines, as well as variations in the thickness and progressive rotation of the forelimb (Allmendinger 1998, Hardy and Ford 1997, Cardozo and Aanonsen 2009, Hardy and Allmendinger 2011, Brandes and Tanner 2014). The trishear method can also approximate the complex strain patterns observed in natural examples (Allmendinger et al. 2004, Liu et al. 2012, Grothe et al. 2014), where strain is highly heterogeneous since it is dependent on the mechanical stratigraphy and the geometry of the main fault (Cristallini and Allmendinger 2001, Allmendinger et al. 2004, Cardozo 2008).

The main variables of the trishear model are (1) the displacement of the hanging block, (2) the propagation/slip ratio, (P/S, being P the propagation of the fault and S the slip on the fault plane) and (3) the apical angle of the trishear zone (Figure 1D, Allmendinger 1998). Trishear fold shape can vary considerably by changing any of these variables, being particularly sensitive to changes in the P/S ratio.

A general method for the derivation of velocity fields consistent with the basic kinematics of the trishear model of fault-propagation folding was presented by Zehnder and Allmendinger (2000). Velocity fields can be written as functions of the position within the deformation zone (Hardy and Ford 1997, Zehnder and Allmendinger 2000). In the original model, the hanging wall moves at a velocity equal to the incremental slip while the footwall is fixed. Inside the triangular zone, particles move according to a velocity field that ensures preservation of area during deformation (Zehnder and Allmendinger 2000, Cardozo et al. 2003). The velocity field was found assuming a gradient for the velocity component parallel to the fault (Vx in trishear coordinate system; Zehnder and Allmendinger 2000) and calculating a velocity component perpendicular to the fault (Vy in trishear coordinate system; Zehnder and Allmendinger 2000), where it satisfies the zero-divergence criterion (area preservation condition) consistent with the velocity conditions at the limits of the triangular shear zone (Zehnder and Allmendinger 2000, Cardozo 2008, Brandenburg 2013). The equations introduced by Zehnder and Allmendinger (2000) enable the construction of velocity fields assuming incompressibility, continuity of the flow, and matching of the basic boundary conditions of the model. The deformation resulting from any of these fields can be obtained by numerical integration.

3. Numerical models

Numerical forward modeling has been used to simulate a wide range of processes from global mantle convection (Bello et al. 2014, Rubey et al. 2017, Colli et al. 2018) to fault-related processes (Nilfouroushan et al. 2012, Brune et al. 2014, Treffeisen and Henk 2020, Luo et al. 2020, Sari 2021). In this study, we apply the open-source code ASPECT (Advanced Solver for Problems in Earth's ConvecTion; Kronbichler et al. 2012, Heister et al. 2017, Rose et al. 2017, Glerum et al. 2018, Sandiford et al. 2021) that solves the conservation equations of momentum, mass and energy for an infinite Prandtl number (i.e., without inertia) using the Boussinesq approximation (i.e., incompressible flow). This finite element code has been originally designed for modeling mantle convection and plume dynamics (Dannberg and Gassmöller 2018, Zhang and Li 2018, Rajaonarison et al. 2020, Steinberger et al. 2020), but it has been significantly extended and was successfully applied to lithosphere deformation (Glerum et al. 2020, Heckenbach et al. 2021, Holt and Condit 2021, Gouiza and Naliboff 2021). The code is characterized by modern numerical methods, high-performance parallelism and extensibility (Glerum et al. 2018). We performed a series of finite element models simulating shortening in a multi-layer viscoplastic sequence to obtain the velocity field during the evolution of simple fault-propagation folds. We evaluate and compare the velocity field and the resulting geometries with those of the previously introduced kinematic trishear model.

The setup of our model is based on previously identified natural examples of fault-propagation folds at the Agrio fold and thrust belt, Andes of Neuquén, Argentina (Rojas Vera et al. 2015, Lebinson et al. 2018). The model domain has a width of 80 km and a height of 15 km (Figure 2). We include three material layers within a two-dimensional domain in the numerical model setup (Figure 2). All layers are initially horizontal. In all the simulations, the lowest layer is 7,5 km thick and has a density of 2700 kg/m^3, an internal friction angle equal to 20°, and 20 MPa of cohesion (Table 1). To prescribe a master reverse fault, we incorporate a thin region of 1.5 km width and 50 km dipping by an angle of 30° in the bottom layer. Within this fault region, the internal angle of friction and the cohesion are reduced to 10° and 2 MPa, respectively. Two 3.75 km thick layers are defined, above the bottom layer (Figure 2). Plasticity parameters for these layers are varied for the different model runs (Table 1). Both beds represent a potentially weaker cover sequence for the fold. In this way, our simulations are comparable with the classical trishear example for fault-propagation folds proposed by Erslev (1991). Introducing this configuration allows for testing how key material parameters (Table 1) affect the resulting kinematic field. The variations in the velocity and strain are studied in the context of a strongly mechanically differentiated sequence including a basement and a cover composed of two different layers.

Insert table 1 here

Insert Figure 2 here

We employ mesh refinement within predefined rectangular domains, such that the material located at the hanging wall of the fault and frontal limb of the structure is resolved with an element size of 125 m, while the corners are only represented by an element size corresponding to 500 m. Overall, our model contains 19,200 active cells, and 950,131 degrees of freedom. All models were run for 20 time-steps of 20,000 years each for a total of 400,000 years of deformation. This required a computation time of 10 hours on 10 cores.

For simplicity, the reference model M1 and most of our alternative models employ uniform viscosity deformation within the upper and intermediate layers, an approach used in many previous numerical models (Schuh-Senlis et al. 2020, Holt and Condit 2021). The viscous flow law used in the bottom layer of our models is based on deformation experiments of wet anorthite (Rybacki et al. 2006). Model M2 assumes that the upper layer consists of evaporites and uses flow law parameters based on experimental salt deformation data (Bräuer et al. 2011, Baumann et al. 2018). We test for the impact of elastic deformation via Model M5, which additionally accounts for a modulus of rigidity of 10 MPa. Brittle deformation takes place where the viscous or visco-elastic stresses exceed the Drucker-Prager yield criterion, whereas the friction angle and cohesion of each model are listed in Table 1. We applied linear frictional weakening such that the plastic strain is used to weaken the plastic yield stress by up to 90% through cohesion and friction for strains larger than 1.5. Furthermore, viscous strain is used to weaken the pre-yield viscosity up to 90% when a strain magnitude of 1.5 is exceeded. Linear strain weakening is a simple, but very effective way to generate realistic fault networks in numerical forward models and has been successfully applied in various tectonics settings (Huismans and Beaumont 2002, Selzer et al. 2007).

Contractional deformation is imposed through velocity boundary conditions, with the left and right sides of the model having a prescribed velocity of 12 mm/year resulting in a total convergence rate of 24 mm/year. Note that for better comparability to the trishear kinematic model, we present velocities in all figures in a reference frame where the right-hand model boundary is fixed. The model features a free surface at the top and free-slip boundary conditions at the base. The temperature is established following a linear gradient from 293 K at the surface to 750 K at the bottom of the model and the boundary temperatures are held constant throughout the model run. For simplicity, radiogenic heating within the layers is not considered.

We conduct a suite of 5 models including our reference Model M1 where both the intermediate and upper layers have uniform viscosity (Table 1) and the density equals 2700 kg/m^3 for all layers. Alternative models M2 to M5 are designed to explore more complex setups by modifying particular aspects of the reference model. Model M2 is identical to M1, except that the upper layer represents an evaporite bed. This is realized by following the viscous flow originally proposed by Bräuer et al. (2011) and changing the plasticity parameters and density value as shown in Table 1. Evaporitic sequences are common in several fault propagation folds identified, such as Filo Morado in Neuquén Basin (Argentina), which was previously modeled as a trishear fold (Allmendinger et al. 2004). Like reference model M1, models M3 and M4 both include two layers with uniform viscosity. Here, the density for the intermediate and upper layers is equal to 2190 kg/m^3. Besides the modification of this property, we also varied plasticity parameters to equal shale and salt rocks. In model M3, the angle of internal friction and cohesion of the upper and intermediate layers are comparable with values measured in shales (Heng et al. 2015) for comparison with the fault propagation folds identified in the Subandean thrust and fold belt of northwestern Argentina, where Silurian and Devonian shales are predominant (Echavarria et al. 2003). In model M4, the plasticity parameters are comparable with values obtained from salt rocks (Liang et al. 2006, Giambastiani 2020). Finally, in simulation M5 elastic deformation is incorporated.

4. Results

We first analyze the development of fault propagation folding and further compare the velocity field and the resulting geometries of our simulations with the theoretical trishear kinematic model (Figure 3). Instantaneous deformation is depicted in terms of the second invariant of the strain rate tensor which is a common way to represent the strain rate magnitude as a scalar value. This value is also used to compute finite strain at each material point, by adding the product of strain rate and time step to the previously experienced finite strain. The strain rate is also used to generate the velocity output from Aspect which hence shows the instantaneous velocity field.

The reference model M1 simulates folding in a cover sequence over a lower layer of uniform strength, where the main reverse fault was established. Deformation localizes in the fault itself, the backthrust, and the limbs of the fold. The backthrust appears in the initial stages of convergence (Figure 3, model M1) and higher strain rate values are observed adjacently, affecting part of the backlimb. Higher strain rate values of the frontal limb are focused especially in the area close to the tip point, where the displacement of the fault is accommodated by the folding.

Concerning kinematics, the velocity vectors mainly consist of a horizontal component (*Vx*) close to the left corner (Figure 3). In the hanging wall there is a progressive rotation of the velocity field, where the vertical component (*Vy*) increases its value. However, as the simulation progresses, the overall velocity field of the hanging wall becomes parallel to the reverse fault. Inside the front limb, the velocity field exhibits another progressive rotation, where both components decrease until reaching minimum values in the footwall of the structure. This area can be considered equivalent to the triangular zone defined by the trishear model, where internal deformation is concentrated (Figure 3, model M1, initial panel). The resultant structure is asymmetric, characterized by the progressive tightening of the fold hinge and steepening of the frontal limb (Figure 3, model M1, advanced panel). In the advanced stages of the model (Figure 3, model M1, advanced panel), deformation is dominated by minor reverse faults similar to forethrusts, which break the upper layer.

Insert Figure 3 here

Alternative models M2 to M5 exhibit an overall similar structural evolution albeit with several distinct differences (Figures 3 & 4). Model M2 investigates the effect of a weak, evaporitic cover layer situated on top of the sequence. Due to the relatively low strength of this layer, more diffuse deformation is observed where higher strain rate values are distributed laterally and are not limited to the main faults. This also leads to a much more symmetric distribution of deformation compared with the other examples (Figure 3, model M2). In further contrast with the previously described model M1, the progressive rotation in the front limb of M2 cannot be well identified. Besides, the velocity magnitude does not decrease in the upper layer, showing the predominance of the vertical component *Vy* even far from the frontal limb (Figure 3, model M2, advanced panel).

In models M3 and M4 (Figure 3), both the intermediate and upper layers have uniform viscosity, but plasticity parameters of model M3 imitate shale rocks (Wyllie and Norrish 1996, Heng et al. 2015) while in model M4 the parameters are equivalent to salt rocks (Gschwandtner and Galler 2018, Giambastiani 2020). Even with these differences, both resulting structures exhibit similar geometry, strain rate distribution, and kinematic velocity fields. The main differences can be found in the advanced stage where model M3 presents minor reverse faults similar to forethrusts, which affect the upper layer like in the reference model M1 (Figure 3). These features, however, do not appear in model M4.

In model M5 we include elastic deformation to evaluate how it affects the resulting fold (Figure 4). The overall deformation pattern does not change if compared to reference model M1. The main difference is that because of the incorporation of elastic deformation, previously rigid blocks are now able to accommodate elastic strain, which is seen by a relative increase in minimum strain rates (Figure 4). The resultant structure is asymmetric, with a higher prevalence of backthrusts. These backthrusts are branched and at advanced stages (Figure 4, advanced panel) all of them are merging at depth with the main fault. As in the case of the reference model M1 (Figure 3), this simulation also develops minor reverse faults similar to forethrusts, which break the upper layer (Figure 4). Velocity vectors show a similar pattern to the reference model M1. Vectors tend to become parallel to the main fault within the hanging wall. Then, the vector field exhibits a progressive rotation where both the horizontal and the vertical components decrease inside the front limb. This area is located in close contact with the tip point at the end of the fault. Generally, the distribution of the strain rate in model M5 is similar to reference model M1, with higher values concentrated in the faults and the intermediate layer.

Insert Figure 4 here

4.1. Comparing fold shape & kinematic field with the trishear theoretical model

For the comparison of a simple propagation fold structure to the theoretical trishear kinematic model we selected the initial stage of the numerical models (Figures 3 & 4, initial panels). In subsequent stages, the main fault increases displacement and is interacting with the front limb, altering the kinematic field inside the triangular zone. Due to this, the first stage is more appropriate to analyze trishear fitting (Figure 5).

Insert Figure 5 here

First, we tested different trishear apical angles (Figure 5), using the development version of Andino 3D software (Cristallini et al. 2021). In all cases, we worked only with symmetric apical angles that were tested every 10-5 degrees. Then, we used the least squares method to verify the theoretical curves obtained in Andino 3D software, comparing them with the geometry of the beds in the numerical models. In this way, we can produce a better fitting of the layers using apical angle values between 60° and 70° for the forelimb (Figure 5). If we compare the resulting curves with the layers in the simulations, we can see that, in general, high apical angles approximate better the geometry of the forelimb. The only case in which the apical angle is lower is found in model M5, where it is equal to 25°. We then extracted the kinematic field from the numerical models and compared it with the theoretical trishear kinematic field (Figure 6) which was generated using the Andino 3D software with the best fitting apical angle as marked in Figure 5.

Figure 6 shows the comparison between the velocity fields of the numerical and the trishear model as arrows (using the theoretical model in Andino 3D, applying the best value for the apical angle obtained after the geometric adjustment) as well as the absolute difference of the velocity magnitudes as an underlain color scale. The angular misfit of the models therefore highlights those sectors that present the greatest differences. However, we want to stress that generally there is very good agreement between both kinematic fields for most model setups.

The greatest differences are concentrated in the backlimb sector, due to the presence of backthrusting. Contrary, in the zone corresponding to the hanging wall, no great differences are observed with both fields being parallel to the main fault. In the trishear zone, it can be seen that model M2 with a flow law corresponding to saline rocks is the one with the best fit, while the M5 model with incorporated elastic deformation has greater differences in this sector. The M4 model, with plasticity parameters corresponding to evaporite rocks, differs from the other models, and is presenting deviations from the trishear model as well. In this case, the forelimb also exhibits negative values corresponding to an anticlockwise rotation, but the difference is bigger compared to the reference model M1 and model M3.

Insert Figure 6 here

The parameter P/S produces stronger changes than the apical angle in the geometry of the beds (Hardy and Allmendinger 2011, Allmendinger 1998). The geometries of our five model setups are quite similar, suggesting in principle that the P/S ratio is the same for all of them. Due to this, this study focused on the apical angle value while P/S was always set equal to 2. However, we do not discard that non-constant P/S ratios or using asymmetric trishear apical angle values could be combined to give similar satisfactory results.

To facilitate comparison between our model groups, we include Table 2 where the maximum and minimum values for the strain rate and the plastic strain for each model are shown (Table 2). We used the same stage as in Figures 5 & 6 (80,000 years), considering only the forelimb sector. Model M5 presents the highest differences but is still comparable to the other simulations.

Insert table 2 here

4.2. Comparing velocity distribution inside the deformation zone

To conduct a detailed comparison to the kinematic model, we plot the velocity distributions of the different simulations within the trishear coordinate system (Figure 1D). The velocity values for the horizontal and vertical components of the vectors were transformed using the equations presented in Figure 1D. The area where both components are plotted is located from the fault tip up to the upper layer, similar to the zoom images in Figure 5. For models M1, M2, M4 and M5 we present two plots, one for *Vx'* (parallel to the main fault, in Figure 7) and *Vy'* (perpendicular to the main fault, in Figure 8). For each plot, we present 3 profiles that cross-cut the deformation zone illustrating the magnitude of *Vx'* or *Vy'*, respectively. Model M3 was not included because the geometric comparison and the velocity fields are very similar to the reference model M1 (Figures 5 & 6).

Insert Figure 7 here

The fault-parallel velocity component *Vx'* is comparable for all our simulations (Figure 7). In all of the models, this component gradually decreases in magnitude until reaching the footwall of the structure, where the velocity vanishes. Higher values are found closer to the tip of the fault in the hanging wall. The profiles closer to the tip of the fault (Figure 7, Profiles A) show an abrupt reduction of *Vx'* magnitude. As the high-strain zone grows, this reduction becomes more gradual (Figure 7, Profiles B & C). Model M4 presents a different pattern, where the high-strain zone is distorted.

Insert Figure 8 here

The fault-perpendicular velocity component *Vy'* shows more variations than *Vx'* across models (Figure 8). In the reference model M1, higher absolute velocity magnitudes are found inside the zone closer to the tip of the fault and in the hanging wall, located on the left side of the plot. Analyzing the profiles, we observed that the magnitude for *Vy'* in profile D is originally high and positive. When plotting the particles inside the trishear zone, the magnitude decreases until reaching negative values. By the middle of the profile, representing the center of the trishear-like area, a maximum absolute value is reached (Figure 8, model M1). In profiles E and F, *Vy'* values are negative from the beginning. The maximum absolute value is reached closer to the center. The distribution is not symmetric across the fault.

For model M2, the difference to the reference model is significant (Figure 8). The zone is more symmetric. In this model, *Vy'* is positive at the beginning of profiles E and F, contrary to the same profiles for reference model M1. Model M4 also shows a minor distortion in the plot (Figure 8, model M4), but the profiles have a similar shape as the ones for model M2 (Figure 8, model M2). The fault-perpendicular velocity component *Vy'* for model M5 follows the same spatial evolution as in model M1 but has overall lower *Vy'* magnitudes (Figure 8, model M5).

5. Discussion

To compare with the trishear theoretical model we compare our numerical geodynamic models to the results of a fault-propagation fold calculated in Andino 3D software. For this, we applied the trishear model with an apical angle equal to 60° (Figure 9), which generated the best fit to approximate the beds in models M1 and M3. The rotation of the coordinate system is the same as in the case of the simulations (Figures 7 & 8). In Figure 9, we also plot both *Vx'* and *Vy'* using the trishear coordinate system as explained in Figure 1D. In general, we find that all simulations exhibit a kinematic field consistent with the trishear kinematic model (Figure 9). However, depending on the rheological parameters, the models show variations from the theoretical field. The triangular zone identified in the frontal limb for each of the folds develops shortly after the simulations began, suggesting that progressive rotation of the velocity vectors dominates the kinematic from the initial stages of the folding. The distribution of the strain is heterogeneous with the maximum values located in the central part of the triangular zone closer to the tip line. This is consistent with the description of trishear zones in previous studies, including experiments performed with analogue models (Mitra and Miller 2013).

Model M1, used as the reference model, consists of two uniform viscosity layers acting like a sedimentary cover over a lower unit with higher strength representing basement rocks. This configuration produces an anticline similar to that proposed by Erslev (1991) in his original trishear model. The distribution of the velocity magnitudes *Vx'* and *Vy'* (Figures 7 & 8, model M1), especially for *Vx'*, is equivalent to the theoretical distribution generated in the trishear method (Figure 9). The greatest difference is located in the left sector, where the distribution is affected by the main inverse fault (Figure 7, model M1). The variations introduced in the rest of the models allow discriminating the effect of each of the parameters involved.

Insert Figure 9 here

Model M2 includes an upper layer with a variation in viscous dislocation creep parameters and plasticity parameters equivalent to evaporite rocks. This layer acts as a salt bed and even though a fault-propagation fold develops, the final shape of the fold is more symmetric (Figure 3). This unit flows from the hinge to the syncline in the frontlimb. Velocity vectors in the frontal limb should have a lower magnitude and be rather parallel to the main fault, as in the rest of the models (Figure 3). However, the kinematic field (Figure 3, model M2) shows an increase in the magnitude of the velocity vectors at the frontlimb, because of the flow of the particles previously described. Besides, the vectors are not parallel to the fault. Both of these observations could explain why in the trishear plot, the perpendicular component to the fault, *Vy'*, is asymmetric and higher absolute magnitudes are located in the upper sector at the hanging wall. The flow described above produces the distortion and explains the pattern observed. Also, the observations presented above explain the difference observed in Figure 6 when subtracting both kinematic fields (theoretical Andino 3D trishear model and numerical model M2, Figure 6). Moreover, as the nature of the material is more prone to viscous flow rather than to brittle failure, the fault is not propagating through it. Because of this, the thrust is not generating the distortion seen in the other *Vx'* plots. In contrast to all other numerical models, the resulting figure for this model M2 is the only one that is truly symmetric (Figure 7, model M2). This model could also be explained by a low P/S ratio, close to 0. This could explain why the vectors located in the footwall exhibit higher magnitudes than the rest of the models. In models M1, M3 and M4 the P/S is greater, closer to 2 since the fault propagates more than twice its slip.

Model M3 has two uniform viscosity layers like reference model M1, the only difference between them being the plasticity parameters that are equivalent to shale rocks. The shape of the folding of both layers can be modeled by applying the same apical angle (60°). Plasticity parameters variations for this case did not produce a significant modification in the geometry of the folding, or of the kinematic field (Figures 5 & 6). Model M4, is also equivalent to model M3 except for the plasticity parameters that belong to salt rock. The folding could be approximated by applying a similar apical angle (65°). However, in this case, we identified differences with the reference model when plotting the perpendicular and parallel components for the velocity vector (*Vy'* & *Vx'* respectively). In both components the distortion observed is bigger, related to the interaction of the frontal thrust, which propagates more rapidly affecting the kinematic field in the frontal zone, even at early stages because of the nature of the material. The same distortion can be observed when subtracting the velocity vector in the numerical model velocity to the velocity vector for the theoretical trishear -applying the apical angle that produced the best geometrical fit (65°)- (Figure 6). Considering the observed deviation from the theoretical field, the trishear method could be applied with greater success for the reconstruction of structures in the early stages of deformation because the propagation of the main fault and the growth of the secondary structures modify the kinematic field, generating deviations with the proposed theoretical model. This leads us to the conclusion that the plasticity parameters of the rocks involved in the folding must be considered for a better understanding. These parameters influence the way the thrusts develop. In rocks where the mechanical behavior favors the rapid propagation of the main fault, the reconstruction of the structure and its kinematic field could differ from the trishear method.

Model M5 is the same as the reference model but with elastic deformation included. Even though brittle deformation mechanisms are dominant at low pressures and temperatures, and plastic deformation is usually assumed for models of fault-propagation folds (Jacquey and Cacace 2020), we included elastic deformation in model M5. The inclusion of elastic deformation modifies the shape of the folding compared to the other models: A low value for the apical angle in the trishear model is needed to approximate the shape of the fold in the visco-elastic-plastic model, while the angle needs to be high for the visco-plastic models. The subtraction of the numerical model kinematic field to the theoretical trishear kinematic field results in stronger differences in the frontal zone (Figure 6, model M5). Other main differences are the higher strain rate values in the bottom layer and more backthrusts.

For simplicity, we employed a constant P/S ratio of 2 for the entire model evolution which resulted in a best fit for all models. However, non-constant P/S ratios could be tested to produce similar results. Regarding this, it must be taken into consideration that P/S is a very sensitive parameter in the geometry of the beds, compared to the apical angle (Allmendinger 1998). Therefore, we focused on the apical angle because the geometry of our models is quite similar. After performing the analysis of the apical angle values, the variations were small: most models exhibit values from 60° to 70°. Hence, we suggest that P/S does not vary significantly between most of our simulations. In model M5, the fault produces a more marked step in the upper layer, suggesting P/S may not have been constant during the development of the folding. The incorporation of elastic deformation to the model furthermore produced a significant change in the geometry of the beds. Previous studies have shown that the apical angle in triangular zones of deformation decreases with increasing heterogeneity of the cover (Hardy and Finch 2007). The relation between cover heterogeneity and the elastic response incorporated into the simulation needs to be demonstrated. Further examples are required to determine how P/S influences the geometry of the structure, as we only performed a limited number of models with different rigidity modulus and in all cases, the geometry of the beds could be approximated by applying low apical angle values.

Preceding models have demonstrated that distortional strain is focused along the fault and backlimb axial surface and distributed throughout a triangular zone ahead of the fault in the structural forelimb (Hughes and Shaw 2015). Our results are similar to those obtained by previous authors: Johnson (2018) pointed out that fault propagation is likely to have an important influence on resultant buckle fold geometry. In the study performed with boundary element modeling (Johnson 2018), the models showed how folds widen as the fault propagates. The same evolution pattern can be observed in our finite element simulations. Regarding the strain distribution, our simulations in general present a pattern very similar to that obtained in the discrete models of mechanically homogeneous sequences (Hughes and Shaw 2015). This general distribution of internal deformation is maintained in all our models, even when the units differ in their mechanical behavior.

6. Conclusions

We constructed finite elements models of fault-propagation folding consisting of 3 layers and a prescribed reverse fault. We conducted several numerical simulations to examine the influence of various factors on the kinematic field and geometry of the fold. The obtained kinematic fields were compared with the trishear theoretical model.

All models, even with significantly different rheology parameters, exhibited similar velocity distributions that can be approximated using trishear. Each model developed a triangular zone where deformation was concentrated and the velocity vectors showed a progressive rotation. However, when plotting the velocity components according to the trishear coordinate system, some models exhibited distortions in the velocity field, which can be attributed to rheological changes such as the incorporation of a saline layer at the top of the sequence that flows in the zone of the forelimb (model M2); the use of plasticity parameters associated with evaporite rocks (model M4) and the generation of secondary structures when taking into account elastic deformation (model M5).

We propose that the greatest variations in the kinematic field with respect to the theoretical model can be found in structures with layers that present parameters equivalent to mechanically weak evaporite rocks. These variations can be identified in the kinematic field and the geometry of the folding and its evolution. In most of our simulations, deformation was dominated by minor reverse faults similar to forethrusts in the advanced stages, breaking the upper layer. However, models M2 and M4 where layers resembling evaporites were included do not develop this type of pattern. All geometries of the layers were approximated by applying the trishear model with high apical angle values of 60°-70°. The incorporation of elastic deformation in the numerical models produced a significant change in the geometry of the beds, where the layers were approximated by applying an apical angle value of 25°. Overall, this result demonstrates a strong effect of the elastic response in the geometry of the folding. This observation is consistent with studies showing that when the heterogeneity of the sedimentary cover increases, the reconstruction of the structure requires applying lower apical angle values (Hardy and Finch 2007).

Our simulations contribute to modeling fault propagation folds where inverse modeling of the structure cannot be performed due to the difficulty of delineating deformed layers. The numerical models carried out in this work allow obtaining more information on longer-term deformation patterns with complex rheologies. By means of the numerical models it is possible to visualize the different stages of development of the fold. In this way, the presence of minor forethrusts and the geometry of the backthrusts can be inferred, contributing to the most accurate reconstruction of fold and thrust belts.

Acknowledgements

Work carried out with the support of a grant from the Agencia Nacional de Promoción Científica y Tecnológica (ANPCyT) BID PICT project 2019–3834. We thank LA. TE. Andes for the academic license of Andino 3D. IDEAN (Instituto de Estudios Andinos Don Pablo Groeber), Consejo Nacional de Investigaciones Científicas y Técnicas (CONICET), and University of Buenos Aires (UBA) are also recognized for their support during this research. The work was supported by the North-German Supercomputing Alliance (HLRN).

We thank the Computational Infrastructure for Geodynamics (geodynamics.org) which is funded by the National Science Foundation under award EAR-0949446 and EAR-1550901 for supporting the development of ASPECT and Anne Glerum for advice during model setup.

The earlier version of this manuscript was greatly improved after constructive comments by two anonymous reviewers. The fruitful comments of the editor are also appreciated.

References

Ahumada, E.A., Costa, C., Gardini, C.E., Diederix, H., 2006. La estructura del extremo sur de la Sierra de Las Peñas-Las Higueras, Precordillera de Mendoza. Assoc. Geol. Arg. 6. 11-17.

Albertz, M., and Lingrey, S., 2012. Critical state finite element models of contractional fault-related folding: Part 1. Structural analysis. Tectonophysics, 576–577, 133–149. https://doi.org/10.1016/j.tecto.2012.05.015

Allmendinger, R.W., 1998. Inverse and forward numerical modeling of trishear fault propagation folds. Tectonics 17, 640–656. https://doi.org/10.1029/98TC01907.

Allmendinger, R., Zapata, T., Manceda, R., Dzelalija, F., 2004. Trishear kinematic modeling of structures, with examples from the Neuquén Basin, Argentina. In: Mc Clay, K. (Ed.), Thrust Tectonics and Hydrocarbon Systems. AAPG Mem., vol.82, pp. 356-371.

Ballato, P., Brune, S., Strecker, M. R., 2019. Sedimentary loading–unloading cycles and faulting in intermontane basins: Insights from numerical modeling and field observations in the NW Argentine Andes. Earth Planet. Sci. Lett., 506, 388–396. https://doi.org/10.1016/j.epsl.2018.10.043

Baumann, T., Kaus, B., Popov, A., 2018. Deformation and stresses related to the Gorleben salt structure: insights from 3D numerical models, Proc. Conf. Mech.Beh. of Salt, SaltmechIX, pp. 15–27.

Bello, L., Coltice, N., Rolf, T., Tackley, P. J., 2014. On the predictability limit of convection models of the Earth's mantle. Geochemistry, Geophysics, Geosystems, n/a-n/a. https://doi.org/10.1002/2014GC005254

Brandes, C., Tanner, D.C., 2014. Fault-related folding: A review of kinematic models and their application., Earth-Science Rev. 138, 352-370. https://doi.org/10.1016/j.earscirev.2014.06.008.

Brandenburg, J.P., 2013. Trishear for curved faults. J. Struct. Geol. 53, 80–94. https://doi.org/10.1016/j.jsg.2013.04.006.

Braun, J., Sambridge, M., 1994. Dynamical Lagrangian Remeshing (DLR): A new algorithm for solving large strain deformation problems and its application to fault-propagation folding. Earth Planet. Sci. Lett., 124(1–4), 211–220. https://doi.org/10.1016/0012-821X(94)00093-X

Bräuer, V., Eickemeier, R., Eisenburger, D., Grissemann, C., Hesser, J., Heusermann, S., Kaiser, D., Nipp, H. K., Nowak, T., Plischke, I., Schnier, H., Schulze, O., Sönnke, J., Weber, J., 2011. Description of the Gorleben site Part 4: geotechnical exploration of the Gorleben salt dome. Die Bundesanstalt Für Geowissenschaften Und Rohstoffe.

Brune, S., Autin, J., 2013. The rift to break-up evolution of the Gulf of Aden: Insights from 3D numerical lithospheric-scale modelling. Tectonophysics, 607, 65–79. https://doi.org/10.1016/j.tecto.2013.06.029

Brune, S., Heine, C., Pérez-Gussinyé, M., Sobolev, S. V., 2014. Rift migration explains continental margin asymmetry and crustal hyper-extension. Nat. Commun., 5. https://doi.org/10.1038/ncomms5014

Brune, S., Williams, S. E., Butterworth, N. P., Müller, R. D., 2016. Abrupt plate accelerations shape rifted continental margins. Nature, *536*(7615), 201–204. https://doi.org/10.1038/nature18319

Cardozo, N., 2008. Trishear in 3D. Algorithms, implementation, and limitations. J. Struct. Geol. 30, 327–340. https://doi.org/10.1016/j.jsg.2007.12.003.

Cardozo, N., Aanonsen, S., 2009. Optimized trishear inverse modeling. J. Struct. Geol. 31(6), 546–560. https://doi.org/10.1016/j.jsg.2009.03.003

Cardozo, N., Bhalla, K., Zehnder, A., Allmendinger, R., 2003. Mechanical models of fault propagation folds and comparison to the trishear kinematic model. J. Struct. Geol. 25, 1-18. https://doi.org/10.1016/S0191-8141(02)00013-5.

Chester, J.S., Chester, F.M., 1990. Fault-propagation folds above thrusts with constant dip. Journal of Structural Geology 12, 903–910. https://doi.org/10.1016/0191-8141(90)90063-5

Coleman, A. J., Duffy, O. B., Jackson, C. A. L., 2019. What is Trishear? https://doi.org/10.31223/OSF.IO/UZHKR

Colli, L., Ghelichkhan, S., Bunge, H.-P., Oeser, J., 2018. Retrodictions of Mid Paleogene mantle flow and dynamic topography in the Atlantic region from compressible high resolution adjoint mantle convection models: Sensitivity to deep mantle viscosity and tomographic input model. Gondwana Research. https://doi.org/10.1016/j.gr.2017.04.027

Cristallini, E., Allmendinger, R., 2001. Pseudo 3-D modeling of trishear fault-propagation folding. J. Struct. Geol. 23. 1883-1899. https://doi.org/ 10.1016/S0191-8141(01)00034-7.

Cristallini, E., Sanchez, F., Balciunas, D., Mora, A., Ketcham, R., Nigro, J., Hernández, J., Hernandez, R., 2021. Seamless low-temperature thermochronological modeling in Andino 3D, towards integrated structural and thermal simulations. J. South Am. Earth Sci. 105 https://doi.org/10.1016/j.jsames.2020.102851.

Dannberg, J., Gassmöller, R., 2018. Chemical trends in ocean islands explained by plume–slab interaction. Proceedings of the National Academy of Sciences, 201714125. https://doi.org/10.1073/pnas.1714125115

Dewey, J.F., 1965. Nature and origin of kink-bands. Tectonophysics 1, 459–494. https://doi.org/10.1016/0040-1951(65)90019-3

Echavarria, L., Hernández, R., Allmendinger, R., Reynolds, J., 2003. Subandean thrust and fold belt of northwestern Argentina: Geometry and timing of the Andean evolution. American Association of Petroleum Geologists Bulletin. https://doi.org/10.1306/01200300196

Erdős, Z., Huismans, R. S., van der Beek, P., 2019. Control of increased sedimentation on orogenic fold-and-thrust belt structure – insights into the evolution of the Western Alps. Solid Earth, 10(2), 391–404. https://doi.org/10.5194/se-10-391-2019

Erslev, E.A., 1991. Trishear fault-propagation folding. Geology 19, 617–620. https://doi.org/10.1130/0091-7613(1991)019<0617: TFPF>2.3.CO;2.

Finch, E., Hardy, S., Gawthorpe, R., 2002. Discrete element modelling of contractional fault- propagation folding above rigid basement fault blocks. J. of Struct. Geol. 25(4), 515–528. https://doi.org/10.1016/S0191-8141(02)00053-6

Finch, E., Hardy, S., Gawthorpe, R., 2004. Discrete-element modelling of extensional fault-propagation folding above rigid basement fault blocks. Bas. Res. 16(4), 467–488. https://doi.org/10.1111/j.1365-2117.2004.00241.x

Gassmöller, R., Dannberg, J., Bredow, E., Steinberger, B., Torsvik, T. H., 2016. Major influence of plume-ridge interaction, lithosphere thickness variations, and global mantle flow on hotspot volcanism—The example of Tristan. Geochemistry, Geophysics, Geosystems, 17(4), 1454–1479. https://doi.org/10.1002/2015GC006177

Giambastiani, M., 2020. Geomechanical Characterization of Evaporitic Rocks. In Soft Rock Mechanics and Engineering (pp. 129–161). https://doi.org/10.1007/978-3-030-29477-9_6

Glerum, A., Brune, S., Stamps, D. S., Strecker, M. R., 2020. Victoria continental microplate dynamics controlled by the lithospheric strength distribution of the East African Rift. Nature Communications, 11(1), 2881.

Glerum, A., Thieulot, C., Fraters, M., Blom, C., Spakman, W., 2018. Nonlinear viscoplasticity in ASPECT: Benchmarking and applications to subduction. Solid Earth, 9(2), 267–294. https://doi.org/10.5194/se-9-267-2018

Gouiza, M., Naliboff, J., 2021. Rheological inheritance controls the formation of segmented rifted margins in cratonic lithosphere. Nature Communications, 12(1), 4653.

Granado, P., Ruh, J.B., 2019. Numerical modelling of inversion tectonics in fold-and-thrust belts. Tectonophysics 763, 14–29. https://doi.org/10.1016/j.tecto.2019.04.033

Granado, P., Ruh, J.B., Santolaria, P., Strauss, P., Muñoz, J.A., 2021. Stretching and Contraction of Extensional Basins With Pre-Rift Salt: A Numerical Modeling Approach. Frontiers in Earth Science 9. https://doi.org/10.3389/feart.2021.648937

Gray, G. G., Morgan, J. K., Sanz, P. F., 2014. Overview of continuum and particle dynamics methods for mechanical modeling of contractional geologic structures. J. Struct. Geol. 59, 19–36. https://doi.org/10.1016/j.jsg.2013.11.009

Grothe, P. R., Cardozo, N., Mueller, K., Ishiyama, T., 2014. Propagation history of the Osaka-wan blind thrust, Japan, from trishear modeling. J. Struct. Geol. 58, 79–94. https://doi.org/10.1016/j.jsg.2013.10.014

Gschwandtner, G. G., Galler, R., 2018. Long-term behaviour of complex underground structures in evaporitic rock mass – Experiences gained from calculations and geotechnical observations. Tunn. Undergr. Sp. Technol., 78, 159–167. https://doi.org/10.1016/j.tust.2018.04.030

Guzofski, C.A., Mueller, J.P., Shaw, J.H., Muron, P., Medwedeff, D.A., Bilotti, F., Rivero, C., 2009. Insights into the mechanisms of fault-related folding provided by volumetric structural restorations using spatially varying mechanical constraints. AAPG Bulletin 93, 479–502. https://doi.org/10.1306/11250807130

Hardy, S., Allmendinger, R.W., 2011. Trishear: A review of kinematics, mechanics, and applications., AAPG Mem. https://doi.org/10.1306/13251334M943429.

Hardy, S., Finch, E., 2007. Mechanical stratigraphy and the transition from trishear to kink-band fault-propagation fold forms above blind basement thrust faults: A discrete-element study. Mar. Pet. Geol. 24, 75–90. https://doi.org/10.1016/j.marpetgeo.2006.09.001.

Hardy, S., Ford, M., 1997. Numerical modeling of trishear fault propagation folding. Tectonics 16, 841–854. https://doi.org/10.1029/97TC01171.

Heckenbach, E. L., Brune, S., Glerum, A. C., Bott, J., 2021. Is There a Speed Limit for the Thermal Steady-State Assumption in Continental Rifts? Geochemistry, Geophys. Geosystems, 22(3). https://doi.org/10.1029/2020GC009577

Heister, T., Dannberg, J., Gassmöller, R., Bangerth, W., 2017. High accuracy mantle convection simulation through modern numerical methods - II: Realistic models and problems. Geophys. J. Int., 210(2), 833–851. https://doi.org/10.1093/gji/ggx195

Heng, S., Guo, Y., Yang, C., Daemen, J. J. K., Li, Z., 2015. Experimental and theoretical study of the anisotropic properties of shale. Int. J. Rock Mech. Min. Sci., 74, 58–68. https://doi.org/10.1016/j.ijrmms.2015.01.003

Holt, A. F., Condit, C. B. 2021. Slab Temperature Evolution Over the Lifetime of a Subduction Zone. Geochemistry, Geophys. Geosystems, 22(6). https://doi.org/10.1029/2020GC009476

Huang, G., Zhang, Z., Zhang, H., Huangfu, P., Li, Z.H., 2020. Development of contrasting folding styles in the western Yangtze block, South China: Insights from numerical modeling. Tectonophysics 792. https://doi.org/10.1016/j.tecto.2020.228579

Hughes, A.N., Shaw, J.H., 2015. Insights into the mechanics of fault-propagation folding styles. Bulletin of the Geological Society of America 127, 1752–1765. https://doi.org/10.1130/B31215.1

Huismans, R.S., Beaumont, C., 2002. Asymmetric lithospheric extension: The role of frictional plastic strain softening inferred from numerical experiments. Geology. https://doi.org/10.1130/0091-7613(2002)030<0211:ALETRO>2.0.CO;2

Jabbour, M., Dhont, D., Hervouët, Y., Deroin, J.P., 2012. Geometry and kinematics of fault-propagation folds with variable interlimb angle. J. Struct. Geol. 42, 212–226. https://doi.org/10.1016/j.jsg.2012.05.002.

Jacquey, A.B., Cacace, M., 2020. Multiphysics Modeling of a Brittle-Ductile Lithosphere: 1. Explicit Visco-Elasto-Plastic Formulation and Its Numerical Implementation. Journal of Geophysical Research: Solid Earth. https://doi.org/10.1029/2019JB018474

Johnson, K. M. 2018. Growth of Fault-Cored Anticlines by Flexural Slip Folding: Analysis by Boundary Element Modeling. J. Geophys. Res. Solid Earth. 123(3), 2426–2447. https://doi.org/10.1002/2017JB014867

Jourdon, A., Kergaravat, C., Duclaux, G., Huguen, C., 2021. Looking beyond kinematics: 3D thermo-mechanical modelling reveals the dynamics of transform margins. Solid Earth, 12(5), 1211–1232. https://doi.org/10.5194/se-12-1211-2021

Khalifeh-Soltani, A., Alavi, S.A., Ghassemi, M.R., Ganjiani, M., 2021. Geomechanical modelling of fault-propagation folds: Estimating the influence of the internal friction angle and friction coefficient. Tectonophysics. https://doi.org/10.1016/j.tecto.2021.228992

Kronbichler, M., Heister, T., Bangerth, W., 2012. High accuracy mantle convection simulation through modern numerical methods. Geophys. J. Int., 191(1), 12–29. https://doi.org/10.1111/j.1365-246X.2012.05609.x

Maillot, B., Leroy, Y.M., 2006. Kink-fold onset and development based on the maximum strength theorem. Journal of the Mechanics and Physics of Solids 54, 2030–2059. https://doi.org/10.1016/j.jmps.2006.04.004

Mitra, S., 1990. Fault-propagation folds: geometry, kinematic evolution, and hydrocarbon traps., American Association of Petroleum Geologists Bulletin. https://doi.org/10.1306/0c9b23cb-1710-11d7-8645000102c1865d

Mitra, S., Miller, J.F., 2013. Strain variation with progressive deformation in basement-involved trishear structures. J. Struct. Geol. 53, 70–79. https://doi.org/10.1016/j.jsg.2013.05.007.

Nilfouroushan, F., Pysklywec, R., Cruden, A., 2012. Sensitivity analysis of numerical scaled models of fold-and-thrust belts to granular material cohesion variation and comparison with analog experiments. Tectonophysics, 526–529, 196–206. https://doi.org/10.1016/j.tecto.2011.06.022

Lebinson, F., Turienzo, M., Sánchez, N., Araujo, V., D'Annunzio, M.C., Dimieri, L., 2018. The structure of the northern Agrio fold and thrust belt (37°30' s), Neuquén Basin, Argentina. Andean Geology 45, 249–273. https://doi.org/10.5027/andgeov45n2-3049

Lebinson, F., Turienzo, M., Sánchez, N., Cristallini, E., Araujo, V., Dimieri, L., 2020. Kinematics of a backthrust system in the Agrio fold and thrust belt, Argentina: Insights from structural analysis and analogue models. Journal of South American Earth Sciences 100. https://doi.org/10.1016/j.jsames.2020.102594

Liang, W. G., Xu, S. G., Zhao, Y. S., 2006. Experimental study of temperature effects on physical and mechanical characteristics of salt rock. Rock Mech. Rock Eng., 39(5), 469–482. https://doi.org/10.1007/s00603-005-0067-2

Liu, C., Yin, H., Zhu, L., 2012. TrishearCreator: A tool for the kinematic simulation and strain analysis of trishear fault-propagation folding with growth strata. Comput. Geosci., 49, 200–206. https://doi.org/10.1016/j.cageo.2012.07.002

Luo, B., Duan, B., Liu, D., 2020. 3D Finite-Element Modeling of Dynamic Rupture and Aseismic Slip Over Earthquake Cycles on Geometrically Complex Faults. Bull. Seismol. Soc. Am., 110(6), 2619–2637. https://doi.org/10.1785/0120200047

Plotek, B., Guzmán, C., Cristallini, E., Yagupsky, D., 2021. Analysis of fault bend folding kinematic models and comparison with an analog experiment. J. Struct. Geol., 146. https://doi.org/10.1016/j.jsg.2021.104316

Rajaonarison, T. A., Stamps, D. S., Fishwick, S., Brune, S., Glerum, A., Hu, J., 2020. Numerical Modeling of Mantle Flow Beneath Madagascar to Constrain Upper Mantle Rheology Beneath Continental Regions. Journal of Geophysical Research: Solid Earth, *125*(2), e2019JB018560. https://doi.org/10.1029/2019JB018560

Richter, M. J. E. A., Brune, S., Riedl, S., Glerum, A., Neuharth, D., and Strecker, M. R., 2021. Controls on asymmetric rift dynamics: Numerical modeling of strain localization and fault evolution in the Kenya Rift. Tectonics, 40, e2020TC006553. https://doi.org/10.1029/2020TC006553.

Rojas Vera, E.A., Mescua, J., Folguera, A., Becker, T.P., Sagripanti, L., Fennell, L., Orts, D., Ramos, V.A., 2015. Evolution of the Chos Malal and Agrio fold and thrust belts, Andes of Neuquén: Insights from structural analysis and apatite fission track dating. Journal of South American Earth Sciences 64, 418–433. https://doi.org/10.1016/j.jsames.2015.10.001

Rose, I., Buffett, B., Heister, T., 2017. Stability and accuracy of free surface time integration in viscous flows. Physics of the Earth and Planetary Interiors, 262, 90–100. https://doi.org/10.1016/j.pepi.2016.11.007

Rubey, M., Brune, S., Heine, C., Davies, D. R., Williams, S. E., Müller, R. D., 2017. Global patterns in Earth's dynamic topography since the Jurassic: the role of subducted slabs. Solid Earth, 8(5), 899–919. https://doi.org/10.5194/se-8-899-2017

Ruh, J.B., 2020. Numerical modeling of tectonic underplating in accretionary wedge systems. Geosphere 16, 1385–1407. https://doi.org/10.1130/GES02273.1

Ruh, J. B., Kaus, B. J. P., Burg, J.-P., 2012. Numerical investigation of deformation mechanics in fold-and-thrust belts: Influence of rheology of single and multiple décollements. Tectonics, 31(3), TC3005. https://doi.org/10.1029/2011TC003047

Rybacki, E., Gottschalk, M., Wirth, R., Dresen, G., 2006. Influence of water fugacity and activation volume on the flow properties of fine-grained anorthite aggregates. Journal of Geophysical Research: Solid Earth, 111(B3), B03203. https://doi.org/10.1029/2005JB003663

Saffar, M. Al, 1993. Geometry of fault-propagation folds: method and application. Tectonophysics 223, 363-380. https://doi.org/10.1016/0040-1951(93)90145-A.

Sandiford, D., Brune, S., Glerum, A., Naliboff, J., Whittaker, J.M., 2021. Kinematics of Footwall Exhumation at Oceanic Detachment faults: Solid-Block Rotation and Apparent Unbending. Geochemistry, Geophysics, Geosystems. https://doi.org/10.1029/2021GC009681

Sanz, P. F., Borja, R. I., Pollard, D. D., 2007. Mechanical aspects of thrust faulting driven by far-field compression and their implications for fold geometry. Acta Geotech., 2(1), 17–31. https://doi.org/10.1007/s11440-007-0025-0

Sari, M., 2021. Secondary toppling failure analysis and optimal support design for ignimbrites in the Ihlara Valley (Cappadocia, Turkey) by finite element method (FEM). Geotech. Geol. Eng. https://doi.org/10.1007/s10706-021-01819-7

Schuh-Senlis, M., Thieulot, C., Cupillard, P., Caumon, G., 2020. Towards the application of Stokes flow equations to structural restoration simulations. Solid Earth. https://doi.org/10.5194/se-11-1909-2020

Selzer, C., Buiter, S. J. H., Pfiffner, O. A., 2007. Sensitivity of shear zones in orogenic wedges to surface processes and strain softening. Tectonophysics, 437(1), 51–70. https://doi.org/10.1016/j.tecto.2007.02.020

Steinberger, B., Bredow, E., Lebedev, S., Schaeffer, A., Torsvik, T. H., 2019. Widespread volcanism in the Greenland–North Atlantic region explained by the Iceland plume. *Nature Geoscience*, *12*(1), 61. https://doi.org/10.1038/s41561-018-0251-0

Suppe, J., Medwedeff, D.A., 1990. Geometry and kinematics of fault-propagation folding. Eclogae Geol. Helv. 83, 409–454.

Treffeisen, T., Henk, A., 2020. Representation of faults in reservoir-scale geomechanical finite element models – A comparison of different modelling approaches. J. Struct. Geol., 131. https://doi.org/10.1016/j.jsg.2019.103931

Van Wijk, J. W., Cloetingh, S. A. P. L., 2002. Basin migration caused by slow lithospheric extension. Earth and Planetary Science Letters, 198(3–4), 275–288. https://doi.org/10.1016/S0012-821X(02)00560-5

Woodward, N. B., 1997. Low-amplitude evolution of break-thrust folding. J. Struct. Geol. 19, 293 - 301.

Wyllie, D., Norrish, N., 1996. Chapter 14: Rock Strength Properties and their measurement. Landslides: Investigation and Mitigation, 372-390.

Zehnder, A., Allmendinger, R., 2000. Velocity field for the trishear model. J. Struct. Geol. 22, 1009-1014. https://doi.org/10.1016/S0191-8141(00)00037-7

Zhang, N., Li, Z. X., 2018. Formation of mantle "lone plumes" in the global downwelling zone — A multiscale modelling of subduction-controlled plume generation beneath the South China Sea. Tectonophysics, 723, 1–13. https://doi.org/10.1016/j.tecto.2017.11.038

Figure Captions:

Figure 1: A. Fault-propagation fold located in Sierra de Las Peñas-Las Higueras (Mendoza Province, Argentina). Note the variations in slip along the fault and how the folding is attenuated in the upper layers (Ahumada et al. 2006). **B.** Cross-section of the northern Agrio fold and thrust belt, located in the Southern Central Andes of Argentina indicating major fault-related folds (Lebinson et al. 2020). **C.** Fault-propagation model by homogeneous, footwall-fixed trishear. The thickness of the beds is not preserved (modified from Erslev 1991). **D.** General trishear geometry. The first analysis considered the footwall completely fixed (modified from Allmendinger 1998). The figure illustrates the conversion from the original coordinate system of the numerical model (*X* and *Y*, in black) to the trishear coordinate system (*X´* and *Y´*, in grey) with $Vx' = \cos(\alpha)\, Vx - \sin(\alpha)\, Vy$ and $Vy' = \sin(\alpha)\, Vx + \cos(\alpha)\, Vy$. Since α designates the fault dip, *Vx'* is parallel to the main fault while *Vy'* is perpendicular to it. The origin of the trishear coordinate system is located at the tip point of the main fault.

Figure 2: Numerical model setup. Parameters for upper and intermediate layers are summarized in Table 1. The highest mesh refinement corresponds to the location of the hanging wall of the fault and frontal limb of the folding, where the element size is 125 m (strong colors). The corners (light color areas) present an element size of 500 m. Compressional velocities are prescribed at the boundaries in the x-direction.

Figure 3: Evolution of the models M1, M2, M3, and M4 showing the second invariant of the strain rate in a color gradient scale and instantaneous velocity vectors relative to the footwall. Two time-steps are selected for each model: the initial stage (80,000 years) and the advanced stage (360,000 years). In close contact with the tip-line, in the middle layer, it is shown how vectors rotate from higher values to almost zero in the footwall. This area (black lines in the initial stage panel for

model M1) is similar to the triangular zone defined by the trishear model, where internal deformation is concentrated.

Figure 4: Evolution of model M5 where elastic deformation was incorporated. The figure shows the second invariant of the strain rate in a color gradient scale and instantaneous velocity vectors relative to the footwall. Two time-steps are selected for the model: the initial stage (80,000 years) and the advanced stage (360,000 years).

Figure 5: Comparison between initial stage numerical results (80,000 years) and trishear kinematic mode calculated with the Andino 3D software. For each model, results for selected apical angles are shown in the right column, where the black color indicates the value that approximates the shape of the layers best for each of the folds.

Figure 6: The panels depict the trishear model kinematic field results in black arrows and the numerical model velocity field in red. Same stage as in Figure 5. The dark grey line represents the main fault. The color gradient represents the resulting difference (in degrees) after subtracting the total component of the velocity vector of the numerical model from the theoretical trishear model. Negative values indicate anticlockwise rotation, while positive values indicate clockwise rotation. The models agree very well in the trishear zone, while greater differences are observed in the backlimb.

Figure 7: A. Scheme indicating the location of the cross-sections. The apical angle and main fault are included as a straight line. The location of the profiles is shown in black lines. The kinematic field corresponds to the numerical model M1. **B.** Numerical model results in trishear coordinate system showing *Vx*' (the component of the velocity vector parallel to the main fault). Same initial stage as in Figures 5 & 6. The trishear- like zone, from the tip line to the bottom of the upper layer

was plotted after changing the coordinate system as explained in Figure 1D. Profiles from A to C show *Vx'* for each model in a direction perpendicular to the main fault. The profile locations are outlined with black lines in the plots of the top row. The boundaries between the bottom, intermediate and upper layers are shown in red and blue dashed lines, respectively.

Figure 8: Numerical model results in trishear coordinate system depicting *Vy'* (the component of the velocity vector perpendicular to the main fault). Same initial stage as in Figures 5 & 6. Profiles from D to F show *Vy'* for each model in a direction perpendicular to the main fault. *Vy'* magnitude is considerably smaller than for *Vx'*. Inside the trishear zone, *Vy'* is always negative. The biggest distortion to the reference model M1 is found in M4. Boundaries between material layers are shown as dashed lines (see Figure 7).

Figure 9: Analysis of a model performed using the Andino 3D software with an apical angle equal to 60°. **A.** Trishear velocity vector field. The apical angle and main fault are included as a straight line. The location of the profiles is shown in black lines. **B.** *Vx'* profiles from trishear zone showing the velocity magnitude in a color gradient scale. Profiles from A to C show *Vx'* and the tendency is considered similar to the one presented in the plots for the numerical simulations, especially for model M2. **C.** *Vy'* profiles from the trishear zone showing the velocity magnitude in a color gradient scale. *Vy'* is the component of the velocity vector perpendicular to the main fault.

Tables:

Table 1: Rheological parameters for the intermediate and upper layers. In all models, the bottom layer and the prescribed fault feature a mafic flow law derived from deformation experiments of wet anorthite (Rybacki et al. 2006) while the fault is initialized through low brittle strength. M1 is the reference model. All models except model M2 involve uniform viscosity layers (marked with

*). The upper layer in model M2 follows the viscous flow law obtained from experimental data for salt (Bräuer et al. 2011, Baumann et al. 2018). Model M5 includes elastic deformation accounting for a modulus of rigidity of 10 MPa.

Table 2: Maximum and minimum values of strain rate (s^{-1}) and plastic strain for all models, for the initial stage (80,000) inside the forelimb (Same area as in Figure 5).

<table>
<tr><th rowspan="2"></th><th colspan="2">M1</th><th colspan="2">M2</th><th colspan="2">M3</th><th colspan="2">M4</th><th colspan="2">M5</th><th colspan="2">ALL MODELS</th></tr>
<tr><th>Upper*</th><th>Intermediate*</th><th>Upper</th><th>Intermediate*</th><th>Upper*</th><th>Intermediate*</th><th>Upper*</th><th>Intermediate*</th><th>Upper*</th><th>Intermediate*</th><th>Bottom</th><th>Fault</th></tr>
<tr><td>Density (kg/m^3)</td><td colspan="2">2700</td><td>2190</td><td>2700</td><td colspan="4">2190</td><td colspan="2">2700</td><td colspan="2">2700</td></tr>
<tr><td>Cohesion (MPa)</td><td>20</td><td>25</td><td>10</td><td>25</td><td colspan="2">30</td><td colspan="2">10</td><td>20</td><td>25</td><td>20</td><td>2</td></tr>
<tr><td>Angle of internal friction (°)</td><td>20</td><td>20</td><td>30</td><td>20</td><td colspan="2">10</td><td colspan="2">30</td><td>20</td><td>20</td><td>20</td><td>10</td></tr>
<tr><td>Prefactor for dislocation creep ($Pa^{-n} s^{-1}$)</td><td>0.5×10^{-22}</td><td>0.5×10^{-20}</td><td>5.21×10^{-37}</td><td>0.5×10^{-20}</td><td>0.5×10^{-22}</td><td>0.5×10^{-20}</td><td>0.5×10^{-22}</td><td>0.5×10^{-20}</td><td>0.5×10^{-22}</td><td>0.5×10^{-20}</td><td colspan="2">7.13×10^{-18}</td></tr>
<tr><td>Constant viscosity</td><td>X</td><td>X</td><td></td><td>X</td><td>X</td><td>X</td><td>X</td><td>X</td><td>X</td><td>X</td><td colspan="2"></td></tr>
<tr><td>temperature -dependent viscosity</td><td></td><td></td><td>X</td><td></td><td></td><td></td><td></td><td></td><td></td><td></td><td colspan="2">X</td></tr>
<tr><td>Viscosity (Pa s) in isoviscous layers</td><td>10^{22}</td><td>10^{20}</td><td>-</td><td>10^{20}</td><td>10^{22}</td><td>10^{20}</td><td>10^{22}</td><td>10^{20}</td><td>10^{22}</td><td>10^{20}</td><td colspan="2">-</td></tr>
<tr><td>Stress exponent for dislocation creep, n</td><td colspan="2">1</td><td>5</td><td colspan="7">1</td><td colspan="2">3</td></tr>
</table>

<table>
<tr><td>Activation energy for dislocation creep (J/mol)</td><td>0</td><td>$54x10^3$</td><td colspan="2">0</td><td>$345x10^3$</td></tr>
<tr><td>Activation volume for dislocation creep (m^3/mol)</td><td>0</td><td>0</td><td colspan="2">0</td><td>$38x10^{-6}$</td></tr>
<tr><td>Modulus of rigidity (MPa)</td><td colspan="3">-</td><td colspan="2">10 (only in M5)</td></tr>
</table>

Model	Strain rate (s^{-1})		Plastic strain	
	Maximum	*Minimum*	*Maximum*	*Minimum*
M1	$6.0x10^{-12}$	$2.1x10^{-19}$	2.33	-0.0330
M2	$5.7x10^{-12}$	$6.5x10^{-19}$	2.29	-0.0096
M3	$6.1x10^{-12}$	$1.6x10^{-19}$	2.32	-0.0134
M4	$6.2x10^{-12}$	$3.4x10^{-19}$	2.28	-0.0129

M5	$5.4x10^{-12}$	$3.7x10^{-17}$	1.96	-0.0094

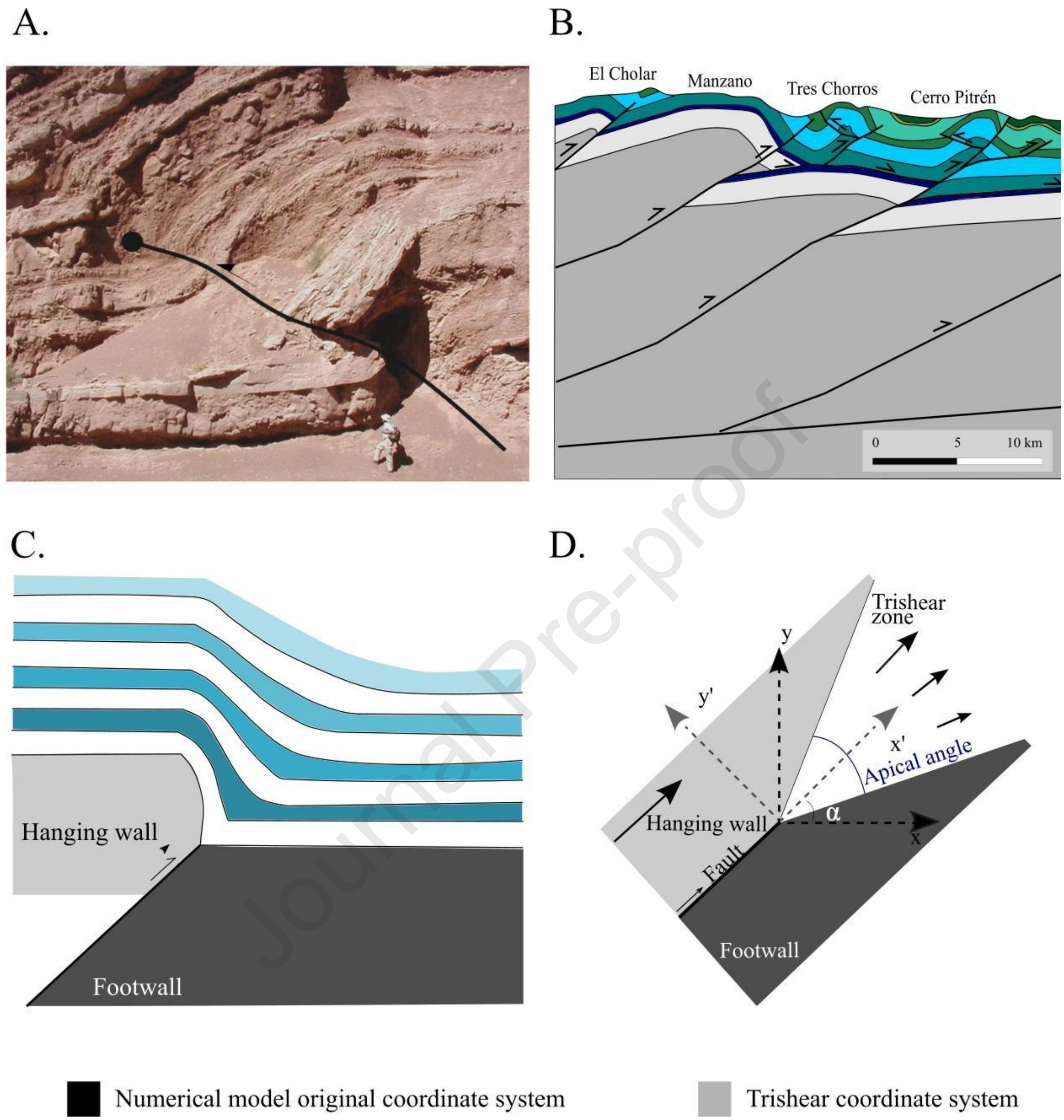

Figure 1: A. Fault-propagation fold located in Sierra de Las Peñas-Las Higueras (Mendoza Province, Argentina). Note the variations in slip along the fault and how the folding is attenuated in the upper layers (Ahumada et al. 2006). **B.** Cross-section of the northern Agrio fold and thrust belt, located in the Southern Central Andes of Argentina indicating major fault-related folds

(Lebinson et al. 2020). **C.** Fault-propagation model by homogeneous, footwall-fixed trishear. The thickness of the beds is not preserved (modified from Erslev 1991). **D.** General trishear geometry. The first analysis considered the footwall completely fixed (modified from Allmendinger 1998). The figure illustrates the conversion from the original coordinate system of the numerical model (*X* and *Y*, in black) to the trishear coordinate system (*X´* and *Y´*, in grey) with $Vx' = \cos(\alpha)\ Vx - \sin(\alpha)\ Vy$ and $Vy' = \sin(\alpha)\ Vx + \cos(\alpha)\ Vy$. Since α designates the fault dip, *Vx'* is parallel to the main fault while *Vy'* is perpendicular to it. The origin of the trishear coordinate system is located at the tip point of the main fault.

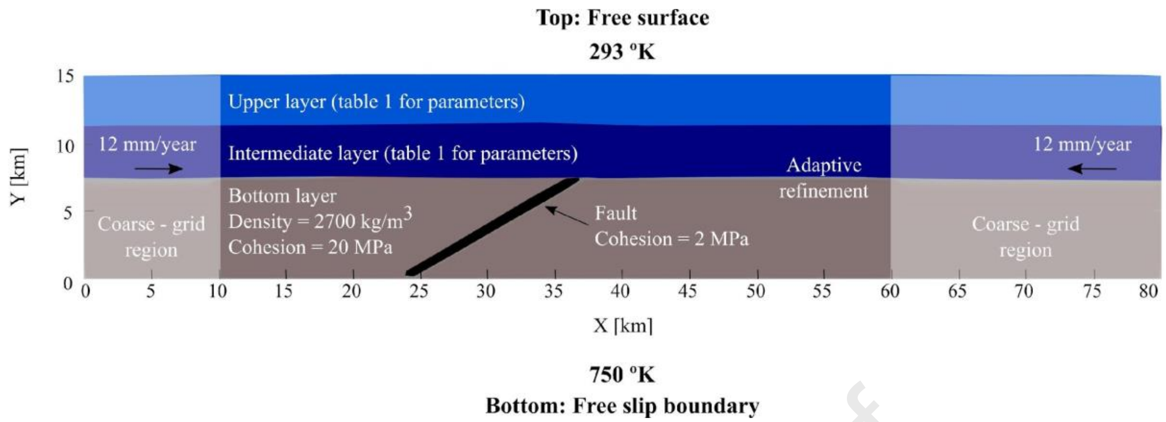

Figure 2: Numerical model setup. Parameters for upper and intermediate layers are summarized in Table 1. The highest mesh refinement corresponds to the location of the hanging wall of the fault and frontal limb of the folding, where the element size is 125 m (strong colors). The corners (light color areas) present an element size of 500 m. Compressional velocities are prescribed at the boundaries in the x-direction.

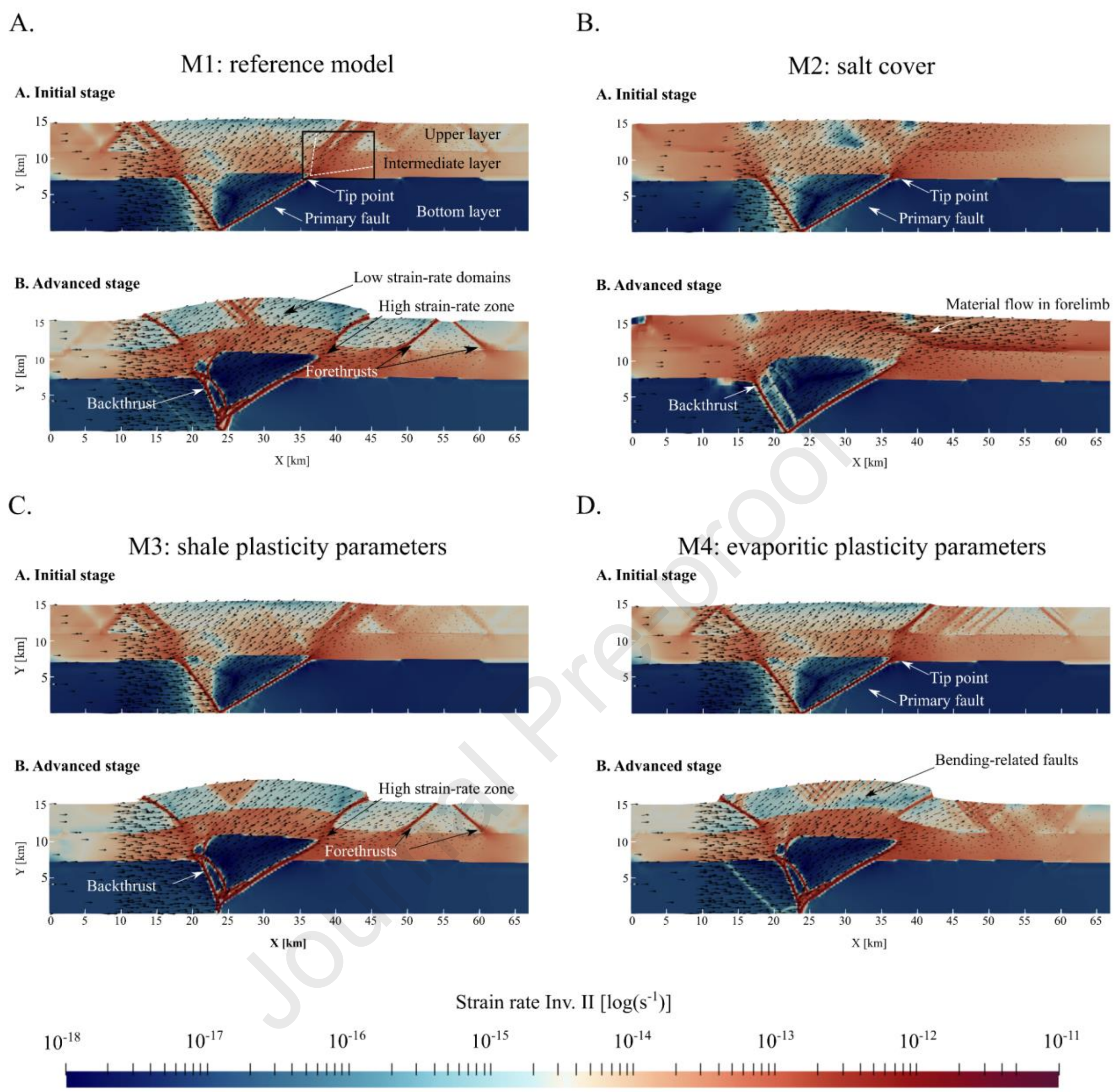

Figure 3: Evolution of the models M1, M2, M3, and M4 showing the second invariant of the strain rate in a color gradient scale and instantaneous velocity vectors relative to the footwall. Two time-steps are selected for each model: the initial stage (80,000 years) and the advanced stage (360,000 years). In close contact with the tip-line, in the middle layer, it is shown how vectors rotate from higher values to almost zero in the footwall. This area (black lines in the initial stage panel for model M1) is similar to the triangular zone defined by the trishear model, where internal deformation is concentrated.

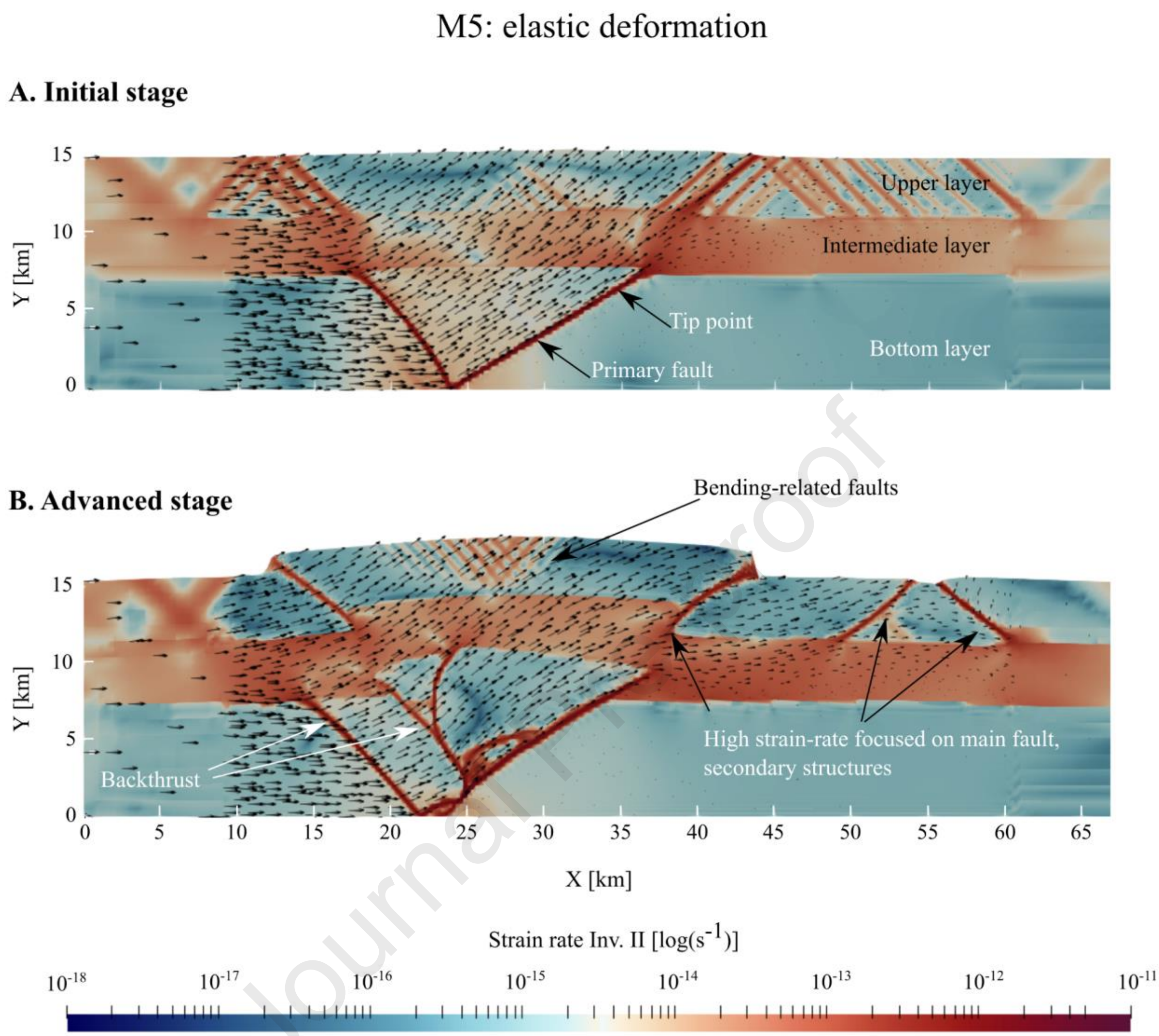

Figure 4: Evolution of model M5 where elastic deformation was incorporated. The figure shows the second invariant of the strain rate in a color gradient scale and instantaneous velocity vectors relative to the footwall. Two time-steps are selected for the model: the initial stage (80,000 years) and the advanced stage (360,000 years).

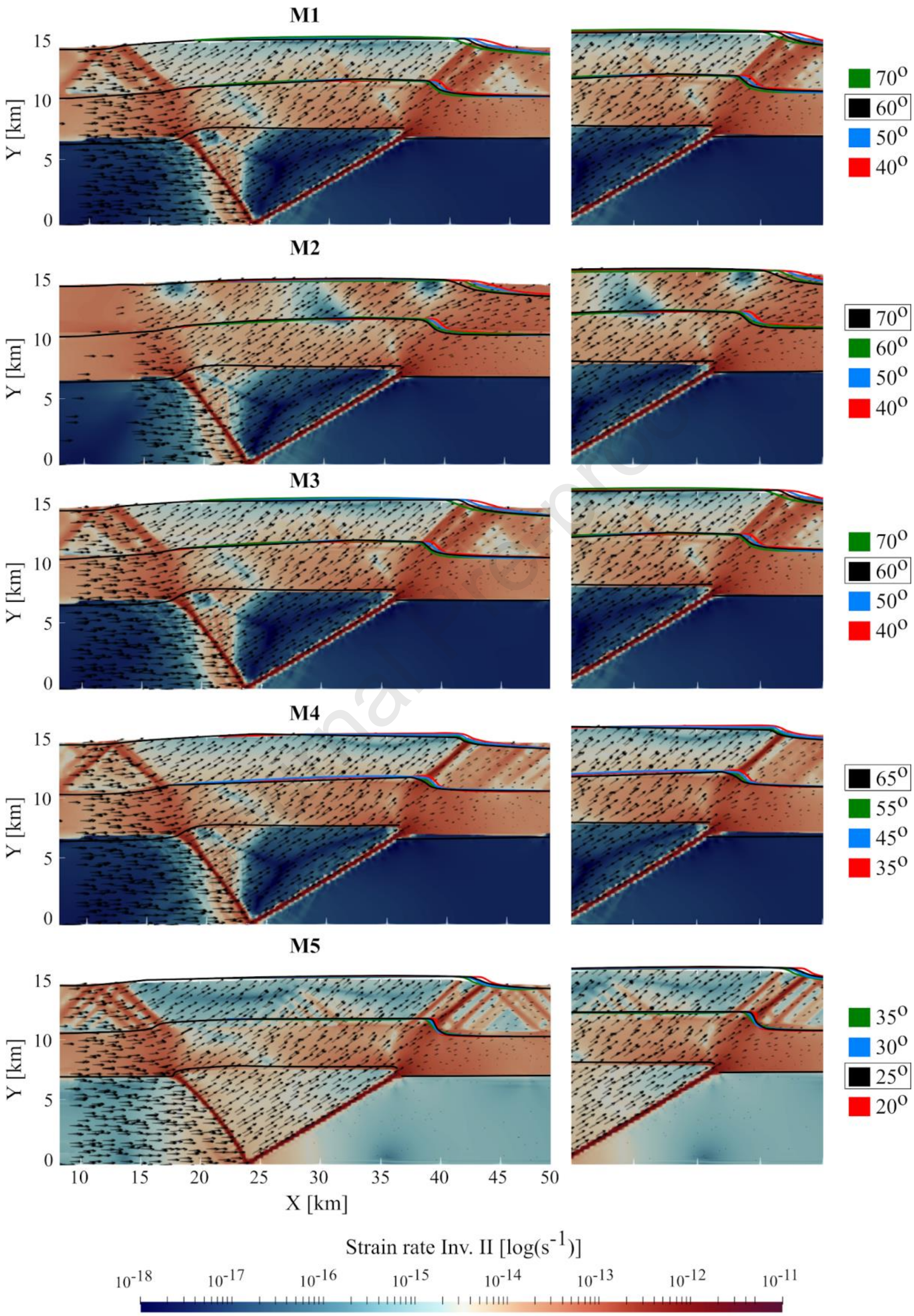
M1
15
10
5
0
Y [km]
70°
60°
50°
40°
M2
70°
60°
50°
40°
M3
70°
60°
50°
40°
M4
65°
55°
45°
35°
M5
35°
30°
25°
20°
10 15 20 25 30 35 40 45 50
X [km]
Strain rate Inv. II [log(s^{-1})]
10^{-18} 10^{-17} 10^{-16} 10^{-15} 10^{-14} 10^{-13} 10^{-12} 10^{-11}

Figure 5: Comparison between initial stage numerical results (80,000 years) and trishear kinematic mode calculated with the Andino 3D software. For each model, results for selected apical angles are shown in the right column, where the black color indicates the value that approximates the shape of the layers best for each of the folds.

Journal Pre-proof

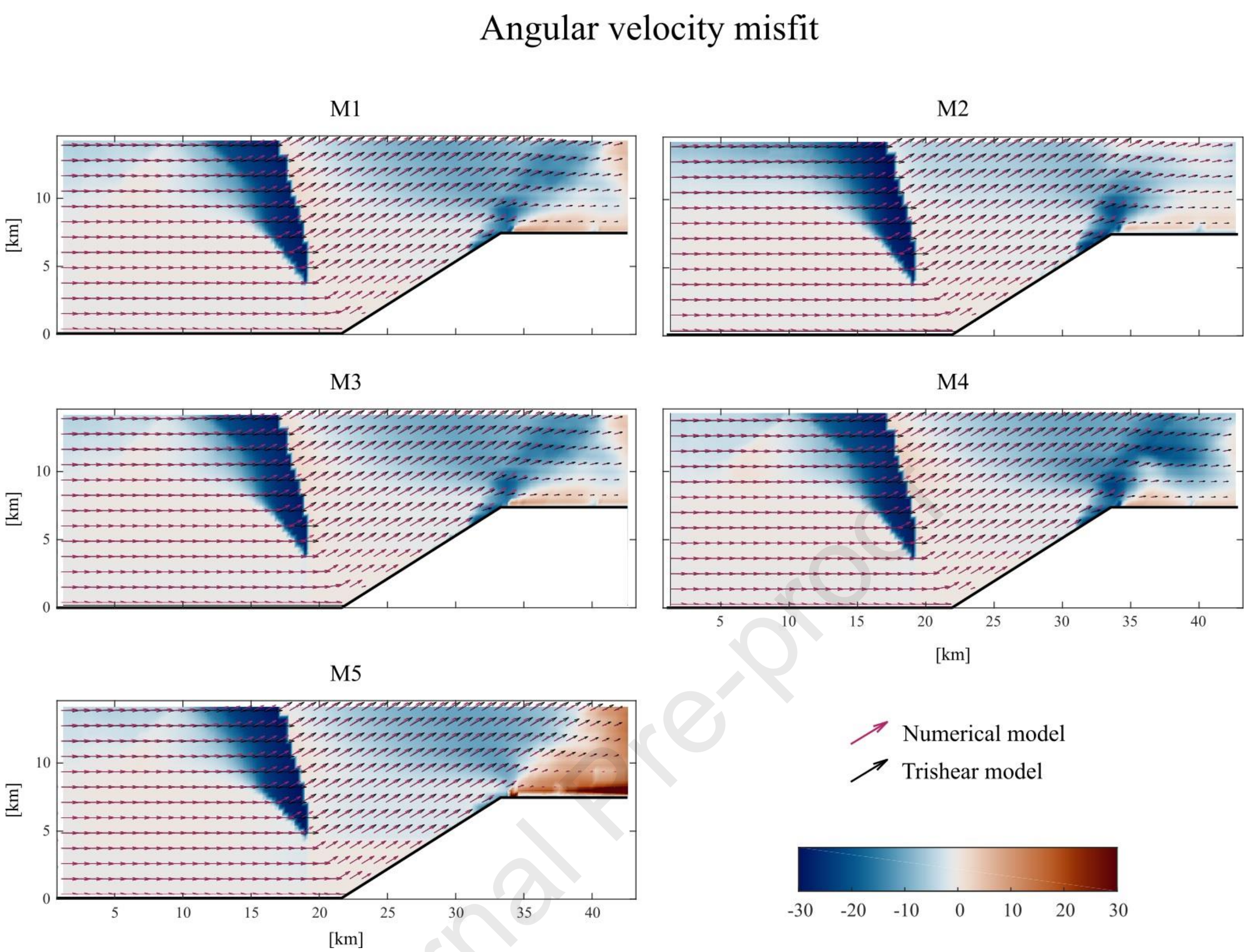

Figure 6: The panels depict the trishear model kinematic field results in black arrows and the numerical model velocity field in red. Same stage as in Figure 5. The dark grey line represents the main fault. The color gradient represents the resulting difference (in degrees) after subtracting the total component of the velocity vector of the numerical model from the theoretical trishear model. Negative values indicate anticlockwise rotation, while positive values indicate clockwise rotation. The models agree very well in the trishear zone, while greater differences are observed in the backlimb.

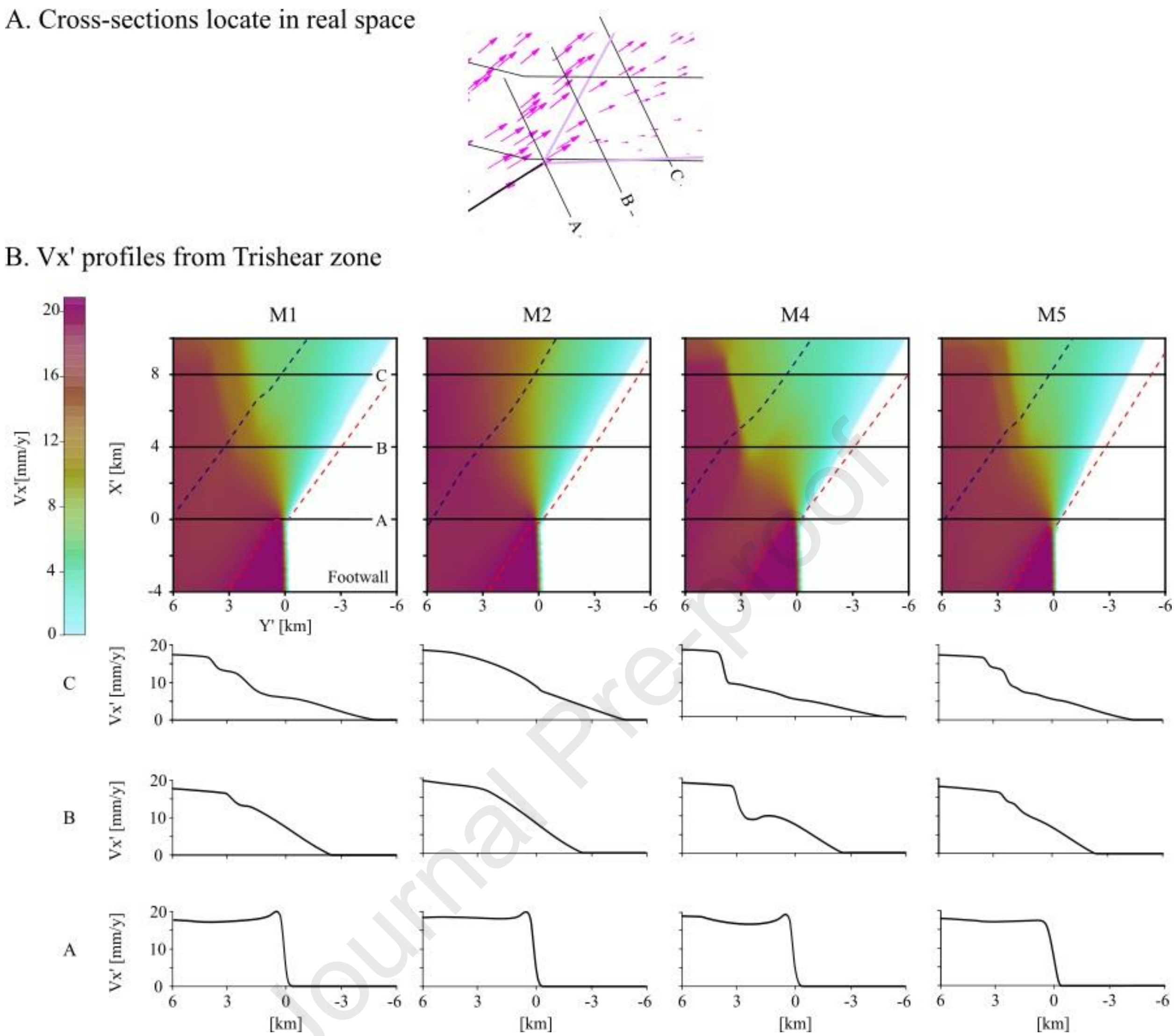

Figure 7: A. Scheme indicating the location of the cross-sections. The apical angle and main fault are included as a straight line. The location of the profiles is shown in black lines. The kinematic field corresponds to the numerical model M1. **B.** Numerical model results in trishear coordinate system showing *Vx*' (the component of the velocity vector parallel to the main fault). Same initial stage as in Figures 5 & 6. The trishear- like zone, from the tip line to the bottom of the upper layer was plotted after changing the coordinate system as explained in Figure 1D. Profiles from A to C show *Vx'* for each model in a direction perpendicular to the main fault. The profile locations are

outlined with black lines in the plots of the top row. The boundaries between the bottom, intermediate and upper layers are shown in red and blue dashed lines, respectively.

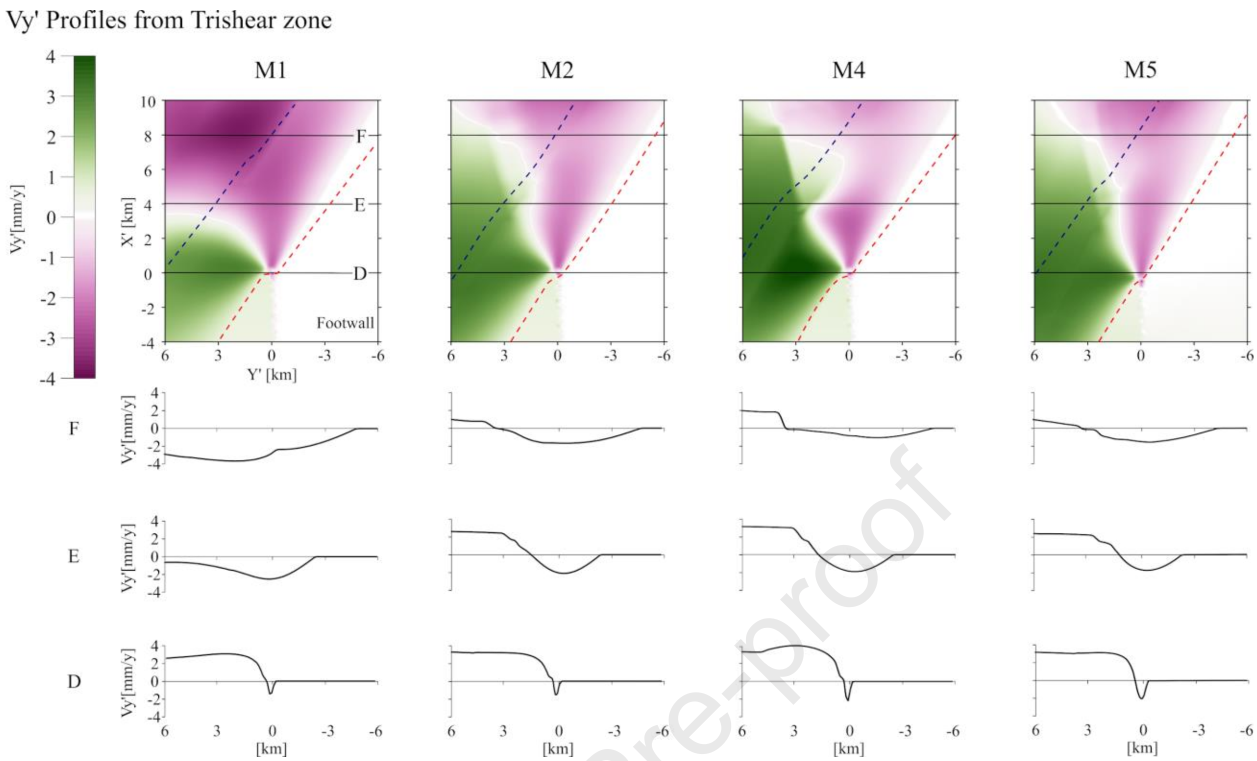

Figure 8: Numerical model results in trishear coordinate system depicting *Vy'* (the component of the velocity vector perpendicular to the main fault). Same initial stage as in Figures 5 & 6. Profiles from D to F show *Vy'* for each model in a direction perpendicular to the main fault. *Vy'* magnitude is considerably smaller than for *Vx'*. Inside the trishear zone, *Vy'* is always negative. The biggest distortion to the reference model M1 is found in M4. Boundaries between material layers are shown as dashed lines (see Figure 7).

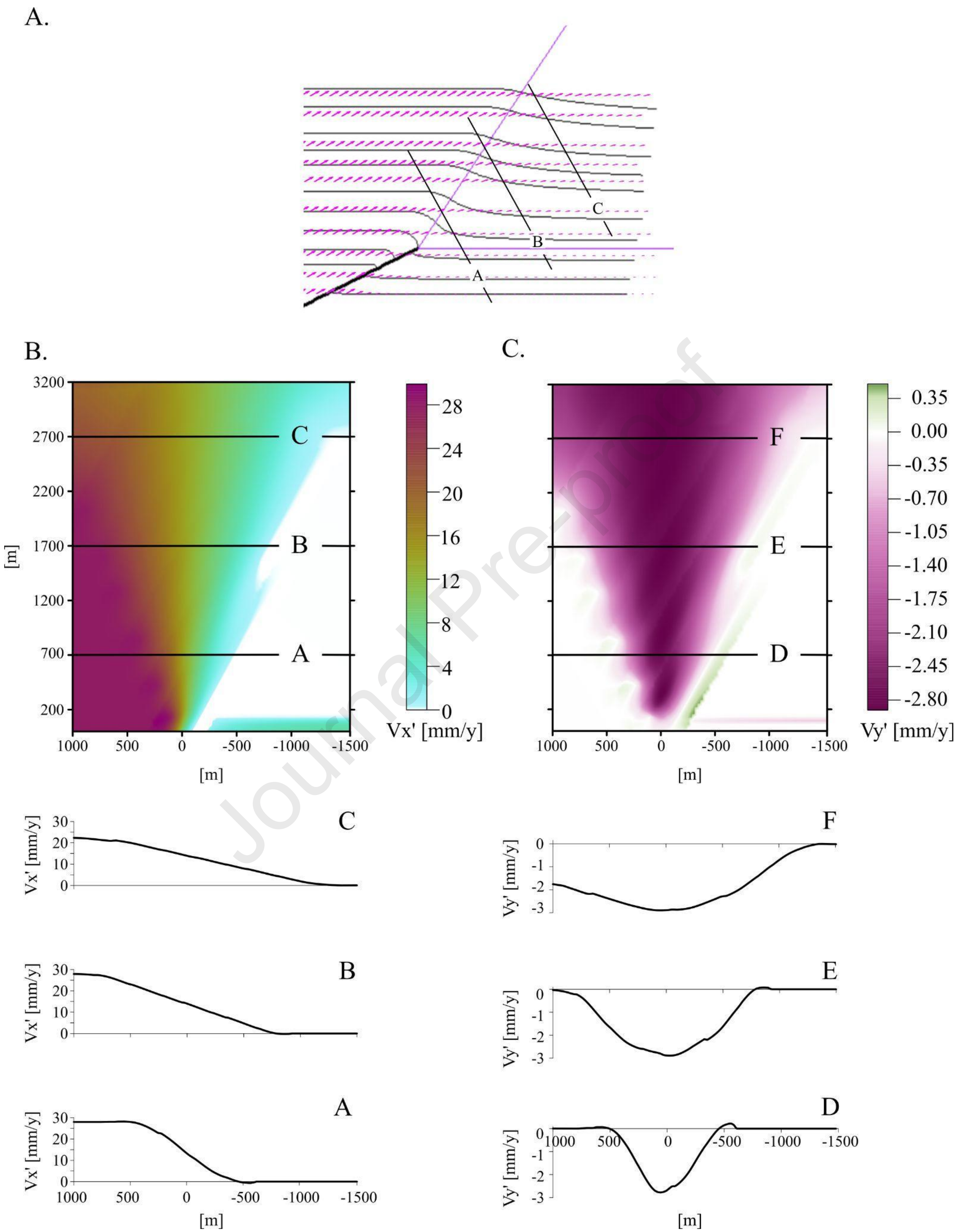
A.
A
B
C
B.
C.
3200
2700
2200
1700
1200
700
200
[m]
1000
500
0
-500
-1000
-1500
[m]
28
24
20
16
12
8
4
0
Vx' [mm/y]
D
E
F
0.35
0.00
-0.35
-0.70
-1.05
-1.40
-1.75
-2.10
-2.45
-2.80
Vy' [mm/y]
Vx' [mm/y]
Vy' [mm/y]

Figure 9: Analysis of a model performed using the Andino 3D software with an apical angle equal to 60°. **A.** Trishear velocity vector field. The apical angle and main fault are included as a straight line. The location of the profiles is shown in black lines. **B.** *Vx'* profiles from trishear zone showing the velocity magnitude in a color gradient scale. Profiles from A to C show *Vx'* and the tendency is considered similar to the one presented in the plots for the numerical simulations, especially for model M2. **C.** *Vy'* profiles from the trishear zone showing the velocity magnitude in a color gradient scale. *Vy'* is the component of the velocity vector perpendicular to the main fault.

81 **Black and white versions:**

82 Figure 1

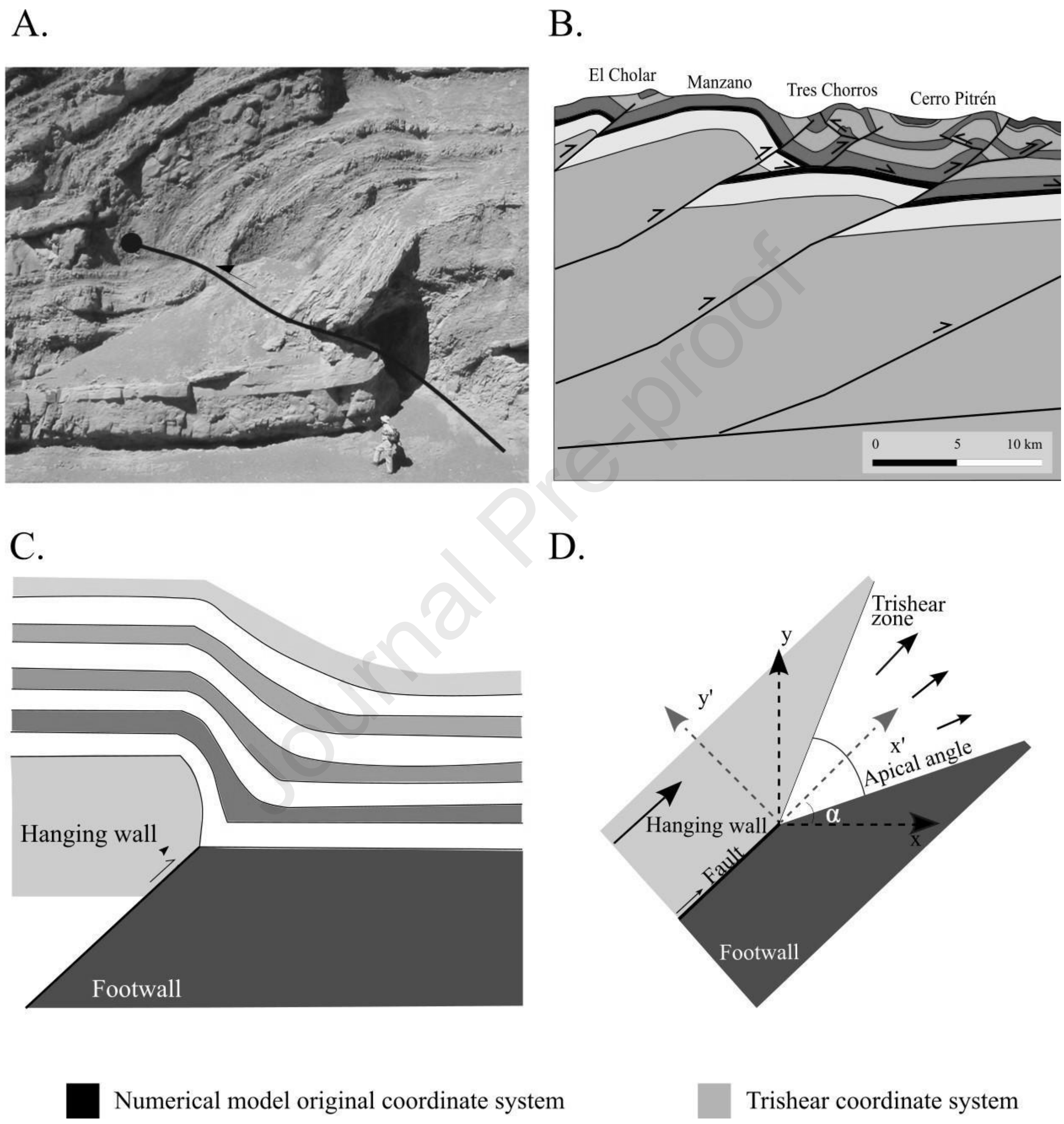

83

84

Figure 2

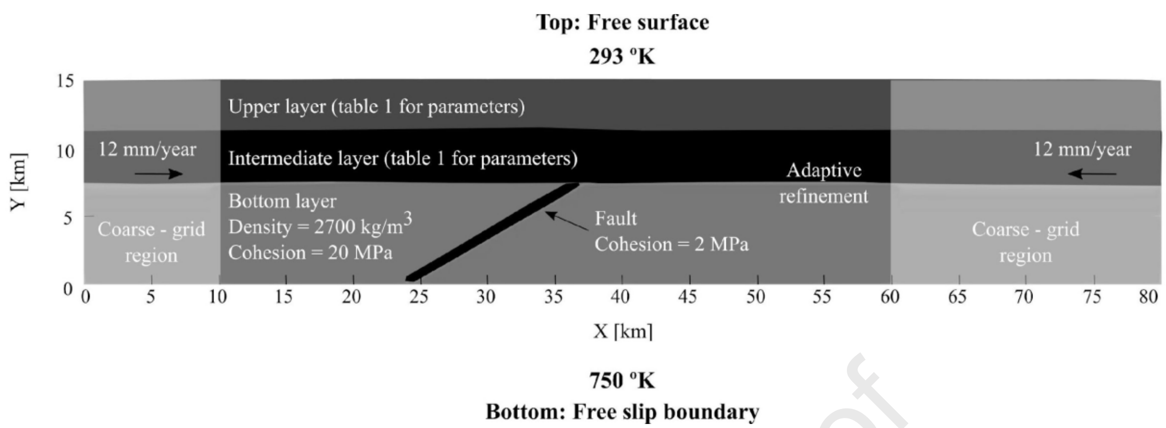
Top: Free surface
293 °K
Upper layer (table 1 for parameters)
12 mm/year
Intermediate layer (table 1 for parameters)
12 mm/year
Adaptive refinement
Bottom layer
Density = 2700 kg/m3
Cohesion = 20 MPa
Fault
Cohesion = 2 MPa
Coarse - grid region
Coarse - grid region
Y [km]
X [km]
750 °K
Bottom: Free slip boundary

Figure 3

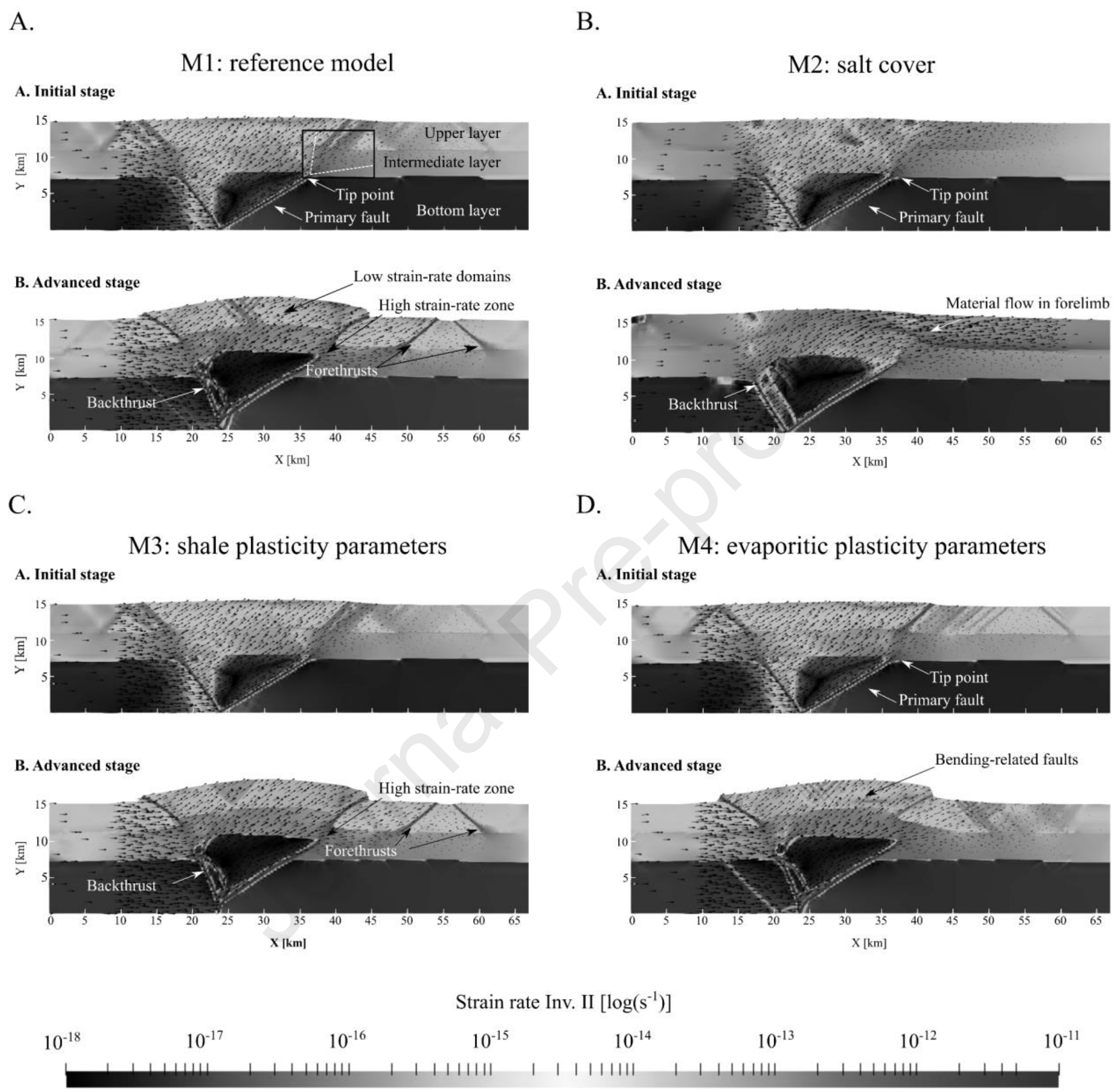
A.
M1: reference model
A. Initial stage
Upper layer
Intermediate layer
Tip point
Primary fault
Bottom layer
B. Advanced stage
Low strain-rate domains
High strain-rate zone
Forethrusts
Backthrust
Y [km]
X [km]
B.
M2: salt cover
A. Initial stage
Tip point
Primary fault
B. Advanced stage
Material flow in forelimb
Backthrust
C.
M3: shale plasticity parameters
A. Initial stage
B. Advanced stage
High strain-rate zone
Forethrusts
Backthrust
D.
M4: evaporitic plasticity parameters
A. Initial stage
Tip point
Primary fault
B. Advanced stage
Bending-related faults
Strain rate Inv. II [log(s-1)]
10-18
10-17
10-16
10-15
10-14
10-13
10-12
10-11

91 Figure 4

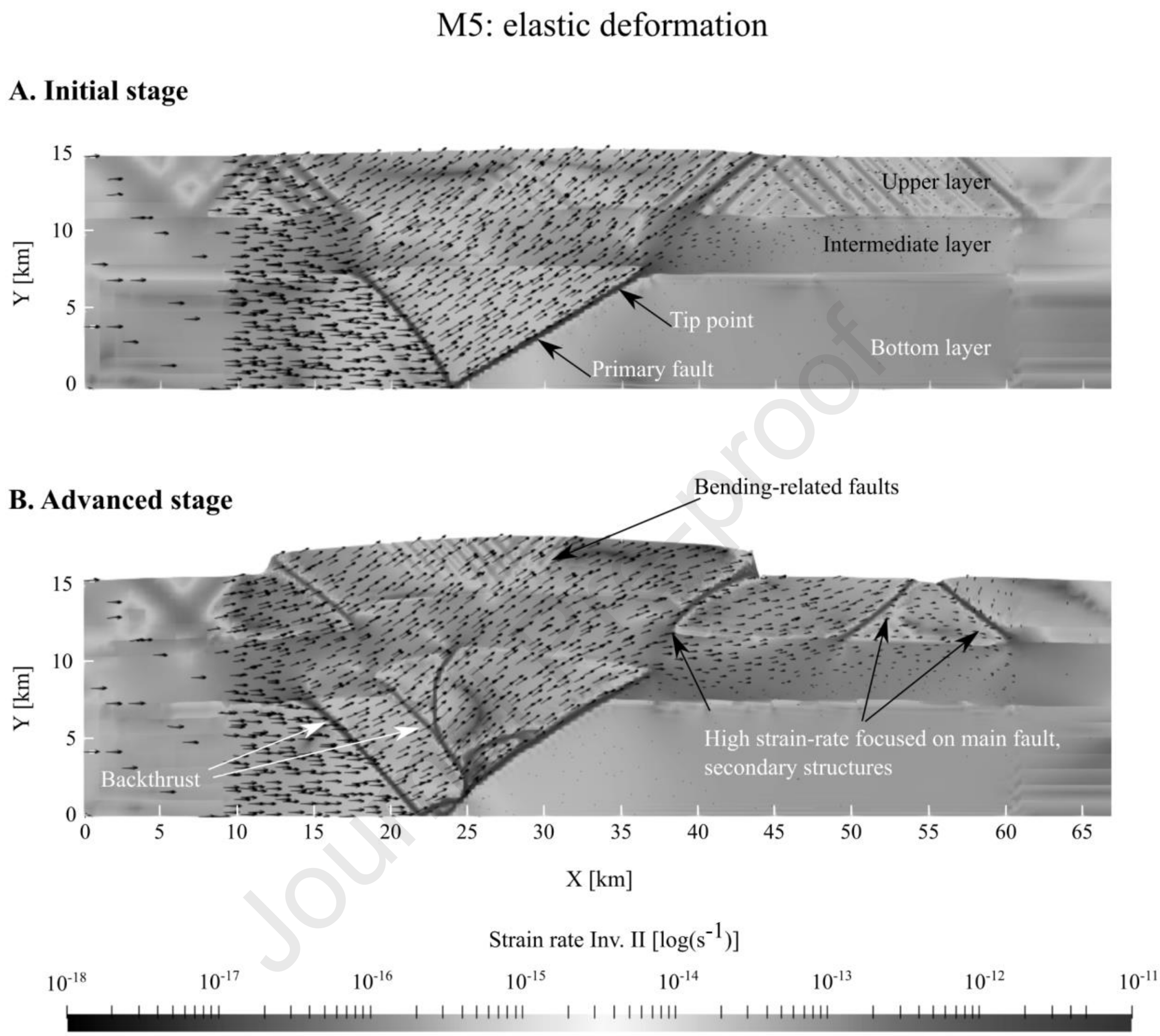

92

93

94 Figure 5

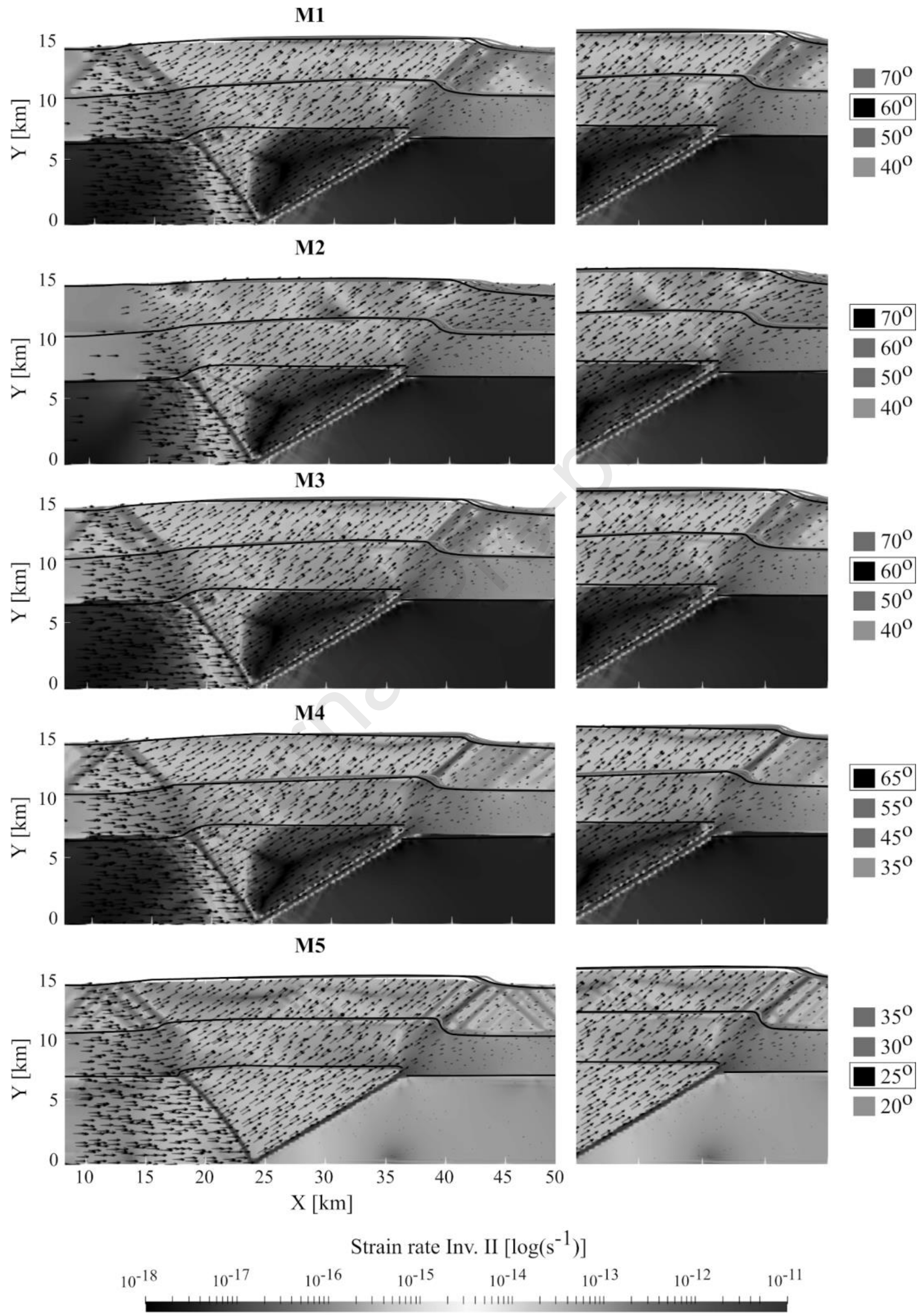

95

96 Figure 6

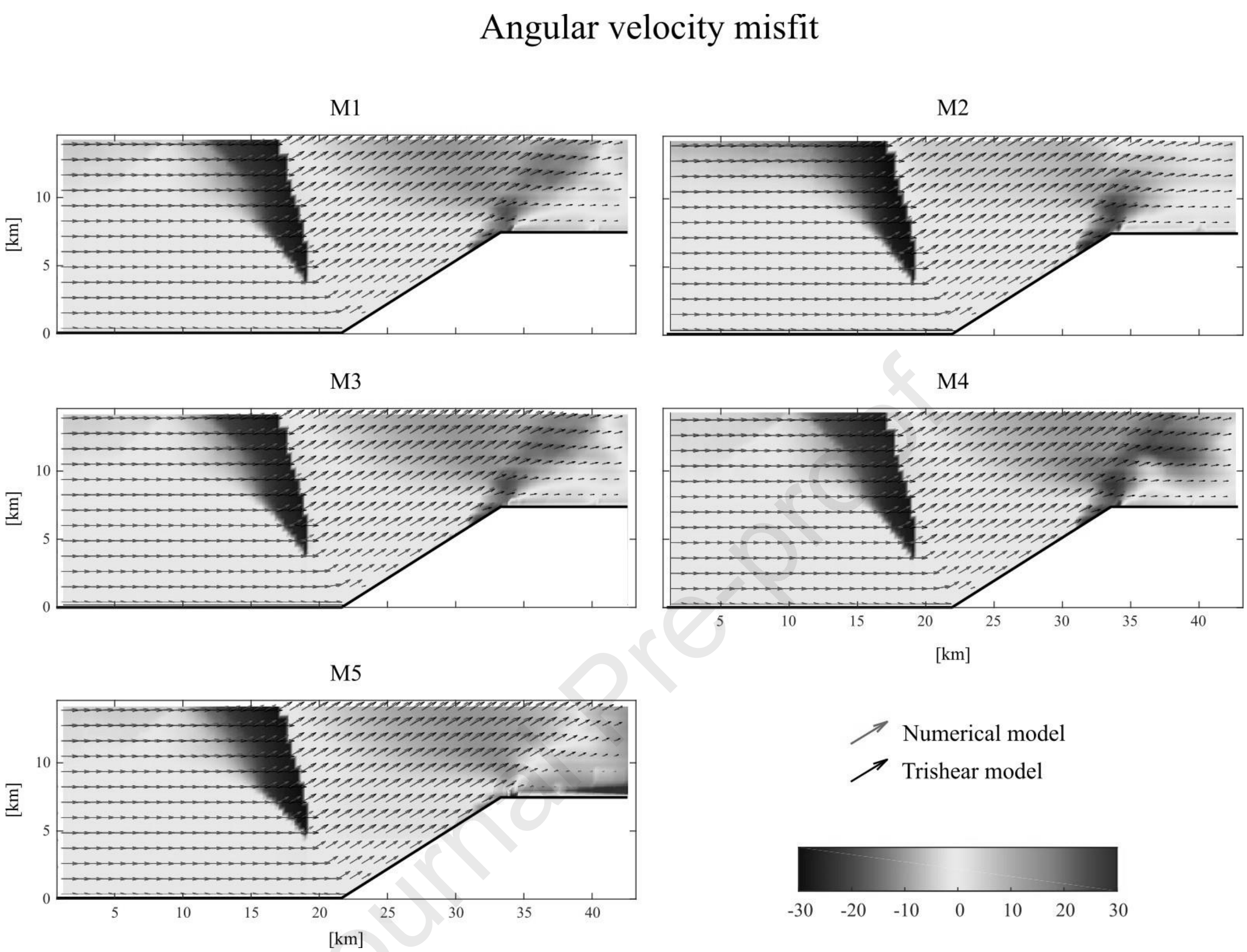

97

98

Figure 7

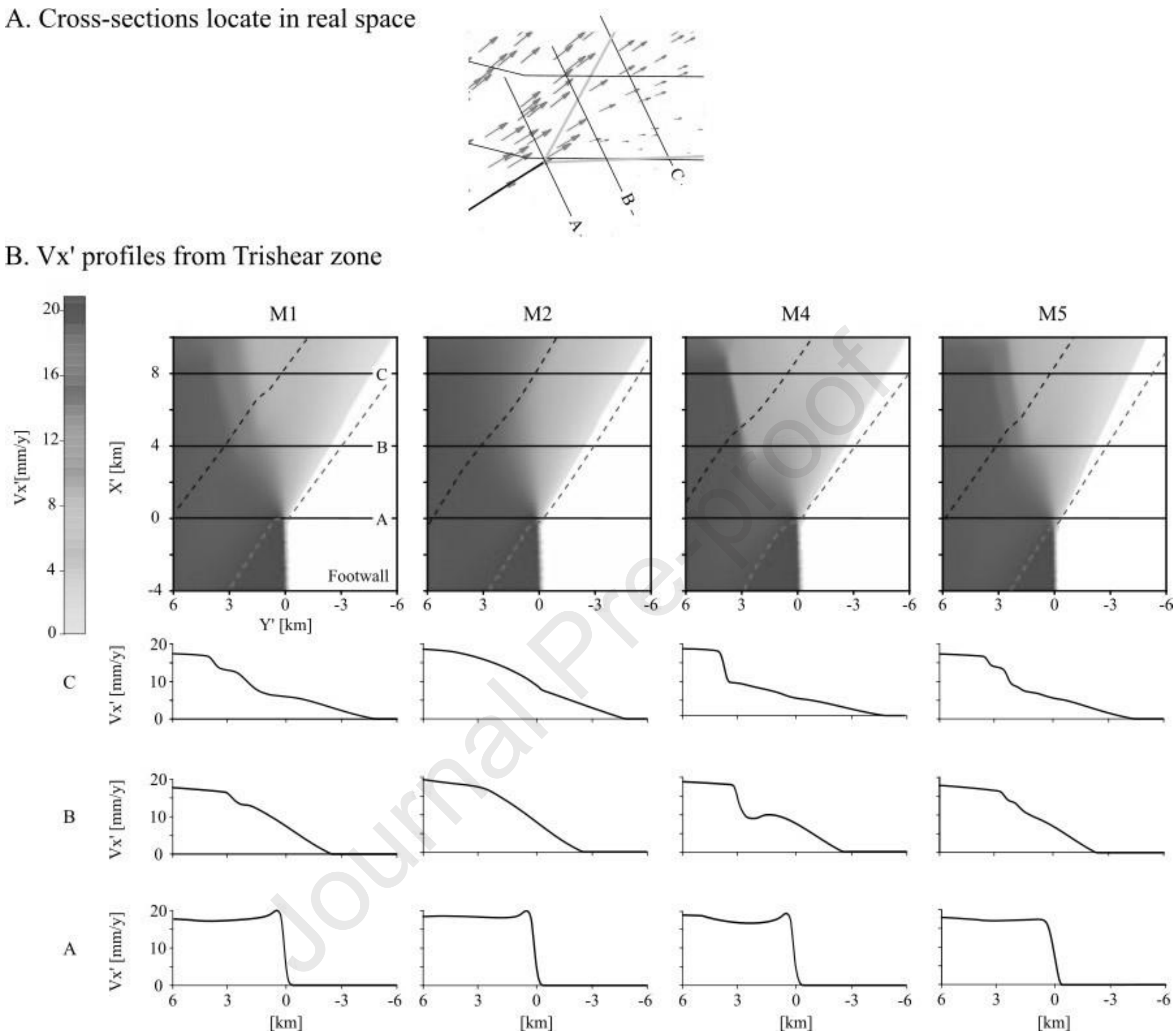
A. Cross-sections locate in real space
A
B
C
B. Vx' profiles from Trishear zone
M1
M2
M4
M5
Vx'[mm/y]
X' [km]
Y' [km]
Footwall
Vx' [mm/y]
[km]

102 Figure 8

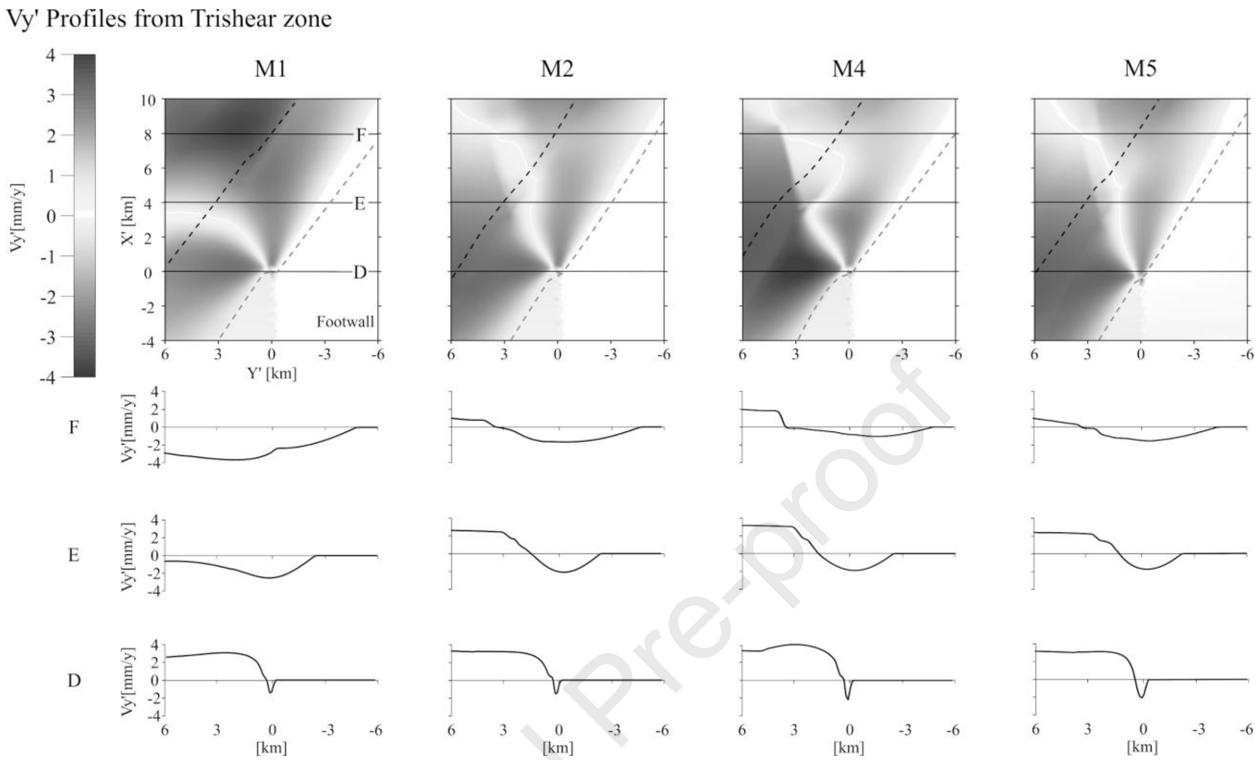

103

104

105 Figure 9

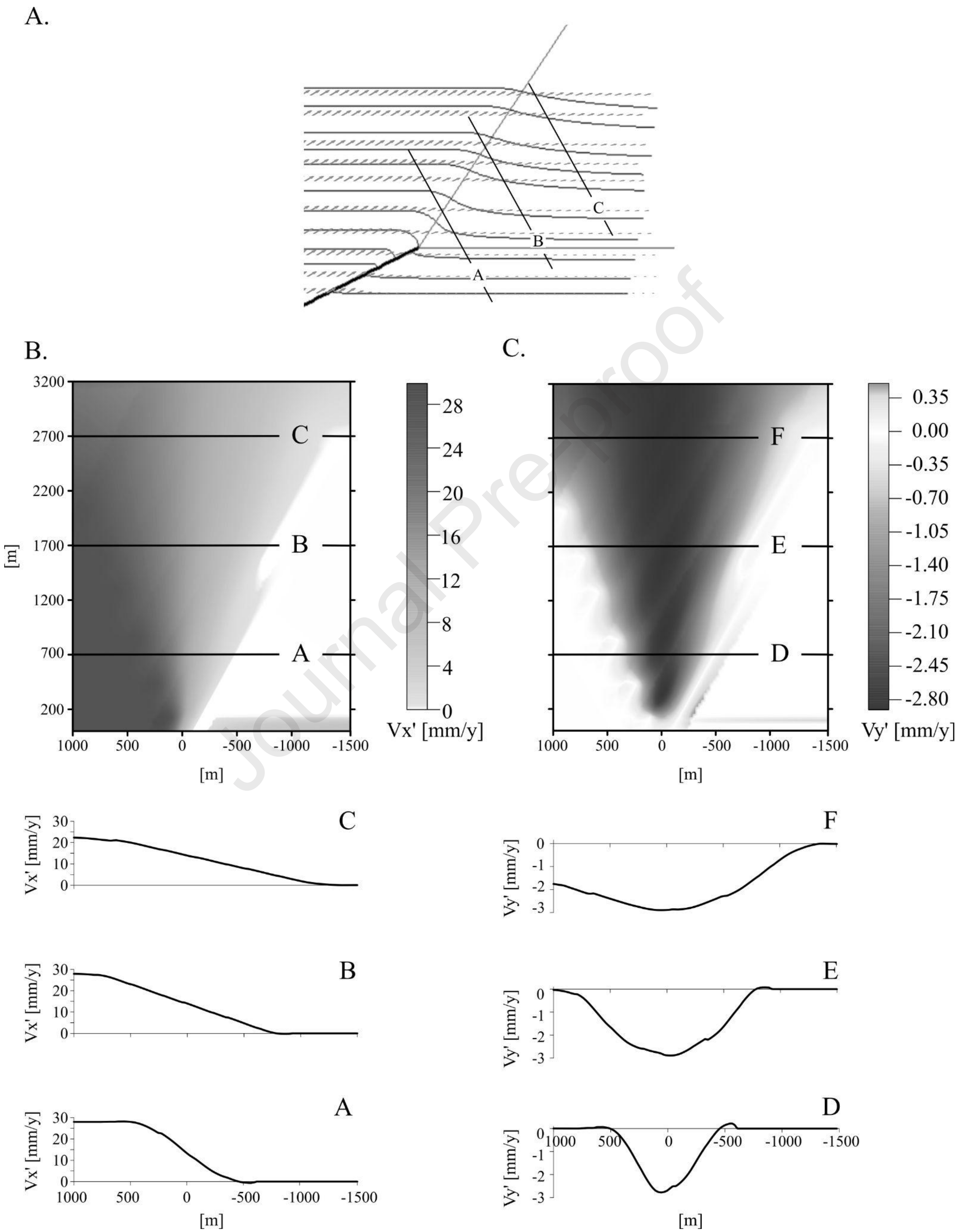

106

Highlights:

- Numerical models were performed to produce fault-propagation folds over an anisotropic sedimentary cover.
- The velocity field during deformation was obtained. Our results were compared with the theoretical kinematic field proposed by the trishear method.
- A triangular region of concentrated strain evolved in all numerical models, even when the layers involved presented strong variations in their rheology.
- In most simulations, deformation was dominated by minor reverse faults similar to forethrusts in the advanced stages, which break the upper unit. Models M2 and M4 where layers resembling evaporites were included, do not develop this type of pattern.
- The geometry of the forelimb obtained can be approximated using a trishear kinematic model with high apical angles.
- The incorporation of elastic deformation in the numerical models produced a significant change in the geometry of the beds.

Plotek: Methodology, Software, Validation, Formal analysis, Investigation, Data curation, Writing – original draft, Writing – review & editing.

Heckenbach: Methodology, Software, Validation, Formal analysis, Investigation, Data curation, Writing – original draft, Writing – review & editing.

Brune: Conceptualization, Methodology, Software, Validation, Formal analysis, Investigation, Data curation, Supervision, Project administration, Funding acquisition, Writing – original draft, Writing – review & editing.

Cristallini: Conceptualization, Methodology, Software, Validation, Formal analysis, Investigation, Data curation, Supervision, Project administration, Writing – original draft, Writing – review & editing.

Likerman: Formal analysis, Writing – review & editing.

Declaration of interests

☒ The authors declare that they have no known competing financial interests or personal relationships that could have appeared to influence the work reported in this paper.

☐ The authors declare the following financial interests/personal relationships which may be considered as potential competing interests: